Ca + HF: The anatomy of a chemical insertion reaction

R. L. Jaffe
NASA Ames Research Center, Moffett Field, California 94035

M. D. Pattengill[a)]
Department of Chemistry, University of Kentucky, Lexington, Kentucky 40506

F. G. Mascarello[b)] and R. N. Zare
Department of Chemistry, Stanford University, Stanford, California 94305

(Received 7 October 1986; accepted 4 February 1987)

A comprehensive first principles theoretical investigation of the gas phase reaction Ca + HF → CaF + H is reported. The overall study involves three distinct elements: (a) generation of an accurate *ab initio* potential energy surface for the ground electronic state of the Ca–F–H system, (b) careful fitting of the computed surface to an analytical form suitable for three-dimensional reactive scattering calculations, and (c) execution of classical trajectory calculations for Ca + HF collisions using the fitted potential surface. *Ab initio* potential energy calculations were performed for 175 Ca–F–H geometries using an MCSCF-CI method with a large Gaussian orbital basis set. The error in the computed endothermicity for the reaction of Ca and HF is less than 1 kcal/mol and the errors in the computed saddle point energies are believed to be less than 3 kcal/mol. The potential energy surface is dominated by a deep well corresponding to a stable linear H–Ca–F intermediate with an extremely small bending force constant. The calculations clearly demonstrate that the preferred geometry for Ca attack on HF is markedly noncollinear. The saddle point for both fluorine exchange reaction and insertion into the H–Ca–F well occurs for a Ca–F–H angle of 75° and has an energy of 16.1 kcal/mol relative to Ca + HF. The energy barrier for collinear reaction, 30.0 kcal/mol, is nearly twice as high. The analytical representation of the *ab initio* potential energy surface is based on a polynomial expansion in the three diatomic bond lengths that reproduces the values of the computed energies to within a root mean square deviation of 1.2 kcal/mol and reduces to the appropriate diatomic potentials in the asymptotic limits. Classical trajectory calculations for Ca + HF($v = 1$) utilizing the fitted surface establish the fact that the H–Ca–F potential well dominates the collision dynamics thus qualifying Ca + HF as a bona fide example of a chemical insertion reaction. Because of the extensive sampling of the H–Ca–F well, many trajectories formed rather long-lived intermediate complexes before reaching diatomic end products. A significant number of these trajectories were not converged with respect to changes in the integration time step. Despite uncertainties associated with the ultimate fates of the nonconverged trajectories, the results obtained support a number of generalizations relating to microscopic features of Ca + HF collisions. Among these are: (1) at fixed total collision energy, excitation of HF to $v = 1$ is much more effective in promoting reaction than is placing the corresponding amount of energy in Ca,HF translation, (2) at fixed initial translational energy, reaction cross sections increase with increasing HF rotational quantum number J, (3) for trajectories which enter the H–Ca–F well, escape to form products is favored by increasing initial HF rotation and escape back to reactants is favored by increasing the initial relative translational energy, and (4) the CaF fractional product energy disposals are remarkably independent of initial collision conditions. These conclusions are compatible with the observation that significant intermode vibrational energy transfer does not occur in the H–Ca–F intermediate on the collision time scale (1–2 ps).

I. INTRODUCTION

Over the past dozen years, the gas phase reactions of alkaline earth metal atoms with hydrogen halide molecules, i.e.,

$$M + HX \rightarrow MX + H \qquad (1)$$

have been studied in great detail. Specific reactions investigated experimentally under single collision conditions include: Ca + HF,[1,3] Ca + HI,[2] Sr + HF,[3–8] Sr + HI,[2] Ba + HF,[6,8–12] Ba + HCl,[9,13,14] Ba + HBr,[9,14] and Ba + HI.[2,9,15] Despite the rather substantial data base provided by these experimental studies, no fully comprehensive theoretical and/or intuitive understanding of the microscopic dynamical features of this class of reactions has emerged.

At moderate collision energies, alkaline earth + hydrogen halide reactions are believed to occur on single potential energy surfaces which are free from complications due to

[a)] John Simon Guggenheim Memorial Foundation Fellow and Visiting Scholar, Stanford University, 1985–86.

[b)] Permanent address: Hoffmann–LaRoche, Abteilung ZFE, BAU 65/605, CH-4002, Basel, Switzerland.

 0021-9606/87/116150-21$02.10

curve crossings, etc. However, the understanding of their dynamics has been hindered by the lack of a simplified underlying conceptual basis. Missing, e.g., are treatments such as those provided by the London equation for covalent reactions of monovalent species and the harpoon mechanism for ionic reactions involving monovalent alkali metal atoms. In addition to complications arising from the existence of a large degree of ionic character, the divalent nature of the alkaline earth atoms opens the real possibility for the existence of energetically stable intermediate complexes of the form H–M–X. To date, the extent of existence and importance of such complex structures (which may lead to nonlinear "reaction coordinates"), their dynamical accessibility and their consequences in terms of observable reaction product attributes have not been examined in any rigorous or exhaustive fashion.

Further complicating the development of reliable theoretical treatments of alkaline earth + hydrogen halide reactions is the fact that the systems most easily accessible to theoretical study (i.e., those containing light alkaline earth atoms) are most inaccessible to experimental characterization and vice versa. Thus, required cross checks between theoretical prediction and experimental observation have been lacking.

Of course, the fundamental construct required for understanding the detailed dynamics of a reactive system is the relevant potential energy surface. Aside from highly simplified one-dimensional treatments of reaction coordinate potential energies,[23,25] with two notable exceptions (*vide infra*) serious theoretical studies of the alkaline earth–hydrogen halide series have focused on the lightest member, Be + HF. Early efforts[16,17] considered rather crude *ab initio* characterization of the collinear Be–F–H reaction pathway and its dynamical characteristics. Later more accurate *ab initio* calculations[21] considered the full three-dimensional Be + HF potential surface and established the existence of a small energetic preference for reaction via a noncollinear Be–F–H reaction pathway, as well as the existence of an energetically stable H–Be–F intermediate. Simultaneous with this development, a series of investigations appeared[18–20] which documented the limited applicability of the semiempirical diatomics-in-molecules method to Be + HF. More recently, two configuration *ab initio* calculations of the collinear Ca–F–H potential profile[24] and a full three-dimensional Mg + HF potential surface[26] have appeared. As in the case of Be + HF, the latter study indicates a weak energetic preference for a noncollinear Mg–F–H reaction pathway and the existence of a stable H–Mg–F intermediate.

The potential surface calculations reported in Refs. 21 and 26, along with the work reported herein (see below) appear to establish nonlinear minimum energy reaction pathways and the existence of stable H–M–X complexes as general features of alkaline earth + hydrogen halide potential energy surfaces. To assess the effects of these features on reaction product attributes, dynamical calculations must be performed. For the sake of meaningful comparisons with experimental data, it is essential that such dynamical calculations employ accurate *ab initio* potential surfaces. In doing this, computed potential points must be fit to a functional form suitable for a fully three-dimensional dynamics calculation. Such a fitting procedure generally involves significant effort, especially for reactions involving a degree of ionic character and, hence, rather abrupt switching between reactants and products. For the case of alkaline earth + hydrogen halide reactions, the full procedure of going from *ab initio* potential to analytical functional fit to full dimensional dynamical calculations has been implemented only for the lightest system,[21,22] Be + HF. Even for this case, however, the accuracy of the *ab initio* calculations coupled with the rather poor quality of the functional fit to them renders the final dynamical calculations capable of qualitative accuracy at best. Further, in the absence of existing and probably future experimental data on the Be + HF reaction, the necessary cross check between the calculations and experimental observation is not possible.

The present work was undertaken to provide a complete study similar in spirit to that previously reported for Be + HF. Of foremost priority was to provide an accurate treatment of an alkaline earth + hydrogen halide system readily amenable to experimental investigation. For this reason, attention was focused on the Ca + HF system which is particularly well suited for the measurement of relative state-to-state reaction cross sections. The process is endothermic for HF $v = 0$ but not for $v = 1$. In fact, no reaction from HF $v = 0$ has been observed.[1,3] In the following, the *ab initio* potential energy calculations are first discussed, along with characteristics of the computed potential energy surface. Next the fitting of the computed potential energy points to a suitable analytical functional form is described and maps of the fitted potential surface are displayed. The methodology and results of a classical trajectory calculation utilizing the fitted potential surface are then presented. Finally, the significance of the trajectory study results are discussed and generalizations concerning dynamical aspects of Ca + HF scattering are drawn.

As will be noted in detail below, the present Ca + HF potential energy surface exhibits marked differences from existing ones[21,26] for Be + HF and Mg + HF. In addition its Ca–F–H collinear profile is in disagreement with that obtained from the previously noted[24] two configuration collinear calculations. As might be expected, the results of the present Ca + HF scattering calculations reveal marked differences from those previously obtained[22] for the system Be + HF.

II. POTENTIAL ENERGY SURFACE CALCULATION

The problem of computing *ab initio* potential energy surfaces has proved to be an exceedingly difficult one.[27,28] In order for the calculation to approach "chemical accuracy" (1 to 2 kcal/mol) an even-handed treatment must be used to describe the reactants, the products, and the interaction region. Accurate calculations have been reported for only a few reacting systems such as $H_2 + H$,[29] $H_2 + F$,[27] and $H_2 + O$.[30,31] Most of these are cases in which collinear approach of the reactants is preferred and the bonding is primarily covalent. Other less accurate potential energy surface calculations (such as existing ones for Be + HF[21] and

Mg + HF[26]) have considered more complicated reactions involving nonlinear reaction coordinates, abrupt covalent to ionic transitions, and intermediate complex formation. The goal of the present study was to determine the lowest potential energy surface for the exchange reaction of Ca atoms with HF to form CaF and H using *ab initio* quantum chemistry methods. This necessitated equivalent descriptions of the bonding in not only CaF and HF, but also in the Ca–F–H interaction region and the possible H–Ca–F molecule.

It is well known that the bond energies of ionic molecules such as CaF can be computed at the SCF level if referenced to the $Ca^+ + F^-$ asymptote provided that a large atomic orbital basis set is used.[32] This result occurs because the electron correlation energy is nearly constant along the ionic molecule potential energy curve (i.e., there is virtually no molecular contribution to the electron correlation energy for an ionic bond). Electron correlation effects must be included, however, for an accurate calculation of the splitting between the ionic and neutral atom asymptotes. Thus, the theoretical determination of the dissociation energy of CaF into neutral atoms requires the accurate calculation of both the Ca atom ionization potential and the F atom electron affinity. Accurate calculation of the HF bond energy is also quite difficult and requires the use of a large atomic orbital basis set and extensive treatment of electron correlation.[33] Unfortunately, even with supercomputers such as the Cray XMP, it is not feasible to design a calculation which simultaneously captures all the above electron correlation effects. As a result, the calculation was designed in such a way that the errors in the computed CaF and HF dissociation energies are nearly equal, leading to an accurate reproduction of the Ca + HF → CaF + H heat of reaction. Hopefully, this even-handedness between the two asymptotic regions of the potential energy surface will extend to the interaction region as well. What follows is predicated on this assumption. As will be shown, although the errors in the CaF and HF dissociation energies are ~9 kcal/mol (cf. Table I), the error in the computed heat of reaction is less than 1 kcal/mol.

The calculations were carried out using the MOLECULE[34]-SWEDEN[35] system of computer codes as implemented at NASA Ames. The atomic orbital basis set employed consisted of contracted Cartesian Gaussian functions equivalent to double zeta for the core electrons and triple zeta for the valence electrons augmented with polarization functions (d on Ca and F and p on H), diffuse p and d functions on Ca, and a diffuse p function on F to better describe the Ca excited states and F^-, respectively. For Ca, the basis set consisted of the (12s,6p,) primitive set given by [36] Roos *et al.*, contracted to (9s,4p) as done[37] by Pettersson *et al.* for their theoretical study of CaH. Added to this set were two diffuse p functions with exponents[37,38] of 0.099 13 and 0.034 64, and a (5d) primitive set contracted[37] to (3d). For F and H, the basis sets used are those given by Dunning[39]: (10s,6p) contracted to (5s,3p) for F and (5s) contracted to (3s) for H. These were augmented[40] with polarization functions ($\alpha_d = 0.9$ for F and $\alpha_p = 1.0$ for H) and a diffuse p function with exponent of 0.074 on F. The resulting (Ca/F/H) primitive basis set is (12s,8p,3d /10s,7p,1d /5s,1p) which has been contracted to (9s,6p,5d /5s,4p,1d /3s,1p). Larger basis sets were considered for calculations of CaF and HF, as discussed below, but it was concluded that this set is well suited to the level of accuracy of calculation used in the present study.

TABLE I. Computed atomic and diatomic properties.[a]

	Present study[b]				
	Ca	F	CaF	HF	CaH
IP	135.9 (136.5)[f]				
EA		70.1 (67.9)[i]			
D_e			118.3 (121.5)[k]	133.0 (131.2)[i]	34.7
r_e			2.01	0.93	2.04
	Larger basis set[c]				
	Ca	F	CaF	HF	CaH
IP	136.0				
EA		72.5[g] (71.2)[i]			
D_e			121.3	135.1[g]	
	Experiment[d]				
	Ca	F	CaF	HF	CaH
IP	140.9[e]				
EA		78.4[h]			
D_e			127.0[j]	141.1	38.3
r_e			1.97	0.92	2.00

[a] Bond lengths are given in Å, energies in kcal/mol.
[b] (9s6p5d /5s4p1d /3s1p) basis set CASSCF and valence CI.
[c] (15s13p7d 2f) contracted to (9s9p6d 2f) for Ca (Ref. 48), same F and H basis as described in the text.
[d] Unless otherwise stated, values from Ref. 44.
[e] C. E. Moore, Ref. 49.
[f] Value in parentheses from CI calculations including all single and double excitations of the Ca 3s, 3p, and 4s electrons.
[g] (5s4p2d) basis set used for F.
[h] H. Hotop and W. C. Lineberger, Ref. 50.
[i] Value in parentheses from CI calculations including all single and double excitations of the F 2s and 2p electrons.
[j] See Ref. 42 for a discussion of CaF dissociation energy.
[k] Ionic dissociation adjusted for computed errors in Ca IP and F EA; the correction is 3.3 kcal/mol for the smaller basis set and 3.5 kcal/mol for the larger one.

An MCSCF calculation known as complete active space SCF or CASSCF[41] in which the Ca 4s and 4p, F 2p, and H 1s orbitals were in the active space was utilized to provide molecular orbitals. This procedure is equivalent to a complete 8 electron/8 orbital MCSCF calculation and yielded 924 configurations in C_s symmetry for the $^1A'$ state. The CASSCF wave function includes the conventional bonding–antibonding interactions as well as the important Ca $4s^2$–$4p^2$ excitations. The core electrons (Ca 1s, 2s, 2p, 3s, and 3p and the F 1s) were described by SCF orbitals obtained for the neutral triatomic and kept frozen in the CASSCF calculations. The F 2s electrons were kept inactive (the orbital was optimized during the CASSCF calculation, but the occupation number was held fixed at 2.0). Care was exercised to insure that the F 2s orbital remained inactive and did not switch with the active Ca 4s orbital.

All the neutral diatomic species relevant to the present study exhibit ionic bonding character. Even in HF, ionic

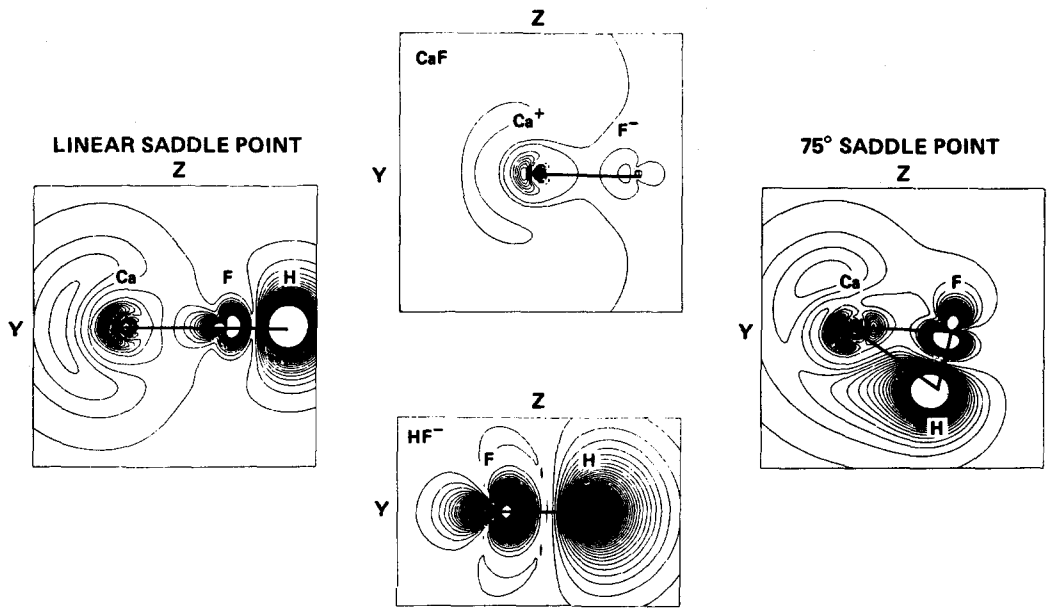

FIG. 1. Valence electron density contours for the Ca–F–H saddle points. The sum of electron density for the 12 a' and 13 a' CASSCF orbitals are shown. The Ca and F atoms lie along the z axis and the H atom lies in the y–z plane. Also shown are the electron densities of the singly occupied orbitals: CaF 8σ (Ca^+4s4p) and HF^- 4σ.

bonding is significant as is reflected by the net atomic charges of ± 0.41 at the equilibrium separation. Bonding in the alkaline earth monohalides is known to be completely ionic.[32,42,43] For CaF, the doubly occupied valence orbitals resemble the F $2p$ shell exclusively. The singly occupied orbital is comprised of highly polarized Ca $4s$ and $4p$ atomic orbitals directed away from the F atom. Owing to the diffuse nature of the latter orbital, a Mulliken population analysis cannot correctly partition the valence electron density between the two atoms. However, the resulting net atomic charges, ± 0.75 at the equilibrium bond length, are still large. CaH exhibits similar bonding,[37] but the bond is much weaker and the Mulliken atomic charges are considerably smaller (± 0.32). The experimental[44] diatomic bond lengths and dissociation energies are given in Table I. Two diatomic ions which have relevance to the Ca–F–H potential energy surface are HF^- which has a purely repulsive ground electronic state and CaH^+ which is predominantly covalent, having a net charge of -0.18 on the H atom at the equilibrium bond length of 1.93 Å.

For collinear Ca–F–H geometries in the saddle point region, the CASSCF wave function has 9 a' and 2 a'' core and inactive orbitals, 2 a' and 1 a'' nearly doubly occupied active orbitals that are mostly F $2p$ in character, a Ca $4s$ + H $1s$ orbital with occupation number of 1.35, and a Ca $4s$–H $1s$ orbital with occupation number of 0.65. There are two dominant closed shell CASSCF configurations: one with coefficient of 0.81 has the Ca $4s$ + H $1s$ orbital doubly occupied and the other, with coefficient 0.57, has the minus combination doubly occupied. As the Ca and H atoms are nearly 3.5 Å apart, this clearly corresponds to unpaired electrons on both atoms. In fact, the Mulliken populations for this geometry show net charges of $+0.78$ on Ca, -0.26 on H, and -0.52 on F. For nonlinear geometries in the saddle point region, the CASSCF wave function is not much different. The Ca $4s \pm$ H $1s$ orbitals have occupation numbers of 1.65 and 0.35, respectively, indicative of the fact that there is now Ca–H σ bonding as might be found in CaH^+. The coefficients of the corresponding CASSCF configurations are 0.90 and 0.40. At this geometry, the atomic charges are $+0.50$ for Ca, -0.50 for F, and 0.00 for H.

Figure 1 shows the combined valence electron densities for the 12 a' and 13 a' CASSCF orbitals at the collinear and bent saddle point geometries. Also shown for comparison are the electron densities of the singly occupied Ca "4s" orbital in CaF and the highest occupied MO in HF^-. At the collinear geometry, the electron density clearly resembles Ca^+ and HF^-. The HF bond is elongated as a consequence of the repulsive nature of the HF^- ion. The collinear and bent saddle points differ only in the apparent stabilization of the HF^- species in the latter case by the establishment of a weak covalent Ca–H bond.

Examination of the atomic charge offers further insight into the nature of the Ca + HF reaction. In the reactants, of course, the Ca atom has no net charge while F and H have charge of -0.5 and $+0.5$, respectively. As the Ca and HF approach, these net charges remain fairly constant as long as the HF bond length stays close to its equilibrium value. If the HF bond is elongated, however, an abrupt electron transfer takes place from Ca to the H atom. Concommitantly, the F charge does not change. Thus, the reaction proceeds as

$$Ca + F^-H^+ \rightarrow Ca^+ - F^- - H \rightarrow Ca^+F^- + H. \qquad (2)$$

For collinear geometries, this electron jump occurs when the HF bond is elongated to 1.31 Å (0.4 Å longer than the equilibrium bond length), while for Ca–F–H angles of 70° to 90° the HF bond elongation is only 0.2 Å beyond the equilibrium value. In both cases, the switch in character is

TABLE II. Reference configurations for CI calculations.

10 a'^a	11 a'^b	12 a'^c	13 a'^d	14 a'^e	15 a'^f	23 a'^g	3 a''^h	4 a''^i
2	2	2	0	0	0	0	2	0
2	2	0	2	0	0	0	2	0
2	2	0	0	0	0	2	2	0
2	2	0	0	0	0	0	2	2
0	2	2	0	2	0	0	2	0
2	2	1	0	0	1	0	2	0
0	2	1	0	2	1	0	2	0

[a] 10 a' F in plane $2p$ orbital directed toward Ca.
[b] 11 a' F in plane $2p$ orbital perpendicular to F–Ca bond.
[c] 12 a' Ca $4s$ in reactants, Ca $4s$ + H $1s$ in interaction region and products.
[d] 13 a' Ca $4p$ in reactants, Ca $4s$–H $1s$ in interaction region and products.
[e] 14 a' F^- $2p'$ in interaction region and products.
[f] 15 a' F^- $2p'$ in interaction region products.
[g] 23 a' Ca $4p$ in reactants (this orbital was not included in the CASSCF active space, but was included in the CI owing to coefficient of 0.075 in test calculations for the reactant's asymptote).
[h] 3 a'' F $2p$ orbital perpendicular to Ca–F–H plane.
[i] 4 a'' F^- orbital in interaction region and products.

quite abrupt and occurs over a range of only about 0.1 Å.

For geometries corresponding to the H–Ca–F molecule, the CASSCF wave function is dominated by a single closed shell configuration with coefficient 0.97, and resembles F^-–$(CaH)^+$. In this molecule, the 10 a', 11 a', and 3 a″ orbitals comprise the F^- $2p^6$ configuration and the 12 a' orbital is a Ca $4s4p$ + H $1s$ σ bonding orbital. The stabilization of the nonlinear saddle point discussed above clearly arises from the same type of bonding seen here for the divalent Ca species.

Following each CASSCF calculation, a multireference configuration interaction (MRCI) calculation was performed using the CASSCF orbitals and a set of reference configurations which represented all the important CASSCF configurations. A configuration was included in the reference set if it had a coefficient of 0.075 or greater in any of several test CI calculations performed for representative Ca + HF, Ca–F–H, F–Ca–H, and CaF + H geometries. There were 7 configurations (given in Table II) in this reference set and the resulting CI consisted of 112 072 CSF'S generated as single and double excitations from these references. Finally, the multireference analog of the Davidson correction[28,45] for the effect of higher order correlation effects was added to all the CI energies. All told, the CASSCF-CI calculations were performed for 175 Ca–F–H geometries (a tabulation of the computed energies is available upon request to RLJ).

The overall calculation can be described as a valence level CASSCF-CI in which the valence space is comprised of Ca $4s$ and $4p$, F $2p$, and H $1s$. It is well known that core–valence effects make an important contribution to the calculation of the Ca ionization potential[32,37] and that more extensive electron correlation effects must be considered in the calculation of the F electron affinity.[46,47] The atomic basis set employed, however, does not include the necessary tight polarization functions needed for treating the Ca $3s3p$ correlation problem. Nor does it include sufficient diffuse and high angular momentum orbitals needed for more accurate calculations on negative ions. It was not deemed feasible to design a manageable calculation that would incorporate all these correlation effects for a nonlinear triatomic molecule. The adequacy of calculations for the diatomic fragments was tested, however, by comparisons with results obtained using a larger basis set.[48]

The computed atomic and equilibrium diatomic properties are given in Table I along with the corresponding experimental values.[44,49,50] It is evident that for the individual species, the agreement with experiment is fairly good. Substantial improvements in the Ca basis set result in almost no change in the computed Ca atom ionization potential and a 3 kcal/mol improvement in the dissociation energy for CaF. Inclusion of core–valence correlation effects is needed for further improvements in these calculated quantities. Additional basis functions and inclusion of higher-order correlation effects are needed to improve the calculated F atom electron affinity and HF bond energy. As can be seen from Table I, inclusion of the F $2s$ electrons in the CI at the singles and doubles level actually increases the error in the computed properties. These augmented calculations would provide more accurate results for the diatomic bond lengths and dissociation energies. However, the computed endothermicity of the reaction is 14.8 kcal/mol which is in excellent agreement with the experimental value of 14.1 kcal/mol. Thus, the errors in the theoretical description of the asymptotic limits are nearly balanced, even though these errors have quite different origins. It is probable that modest improvements in the calculation to correct some of the deficiencies in the description of the diatomic species would result in a substantially larger error in the computed endothermicity.

Calculations were first performed for collinear arrangements of the three atoms. For Ca–F–H, the saddle point is located at $r_{CaF} = 2.12$ Å and $r_{HF} = 1.35$ Å and is 30.0 kcal/mol above the Ca + HF asymptote as referenced to the minimum in the HF potential energy curve. This value is considerably higher than the experimentally observed threshold for reaction to form CaF. Next, a series of calculations was performed in which the Ca–F–H angle was varied while holding the CaF and HF bond lengths fixed at the collinear saddle point values. It was found that the energy dropped rapidly for decreasing angle and achieved a minimum value of 16.1 kcal/mol at 75°. Energies were then computed for a grid of CaF and HF bond lengths with a Ca–F–H angle of 75°. Surprisingly, the saddle point was located at the same bond lengths as on the collinear potential energy surface. The resulting saddle point energy is 1.3 kcal/mol greater than the asymptotic product energy and is consistent with the experimental observation that reaction proceeds with little or no activation energy above the endothermicity.

Figure 2 is a contour plot generated from a two-dimensional cubic spline representation of the computed 75° potential energy surface. Note that there is a rather deep well in the products channel which makes the barrier much more pronounced and narrower than expected. This potential well actually corresponds to the energy of H–Ca–F for extremely small H–Ca–F angles (i.e., 30°–40°). In fact, it is energetically downhill from both the saddle point and the product well geometry to the equilibrium structure of the divalent cal-

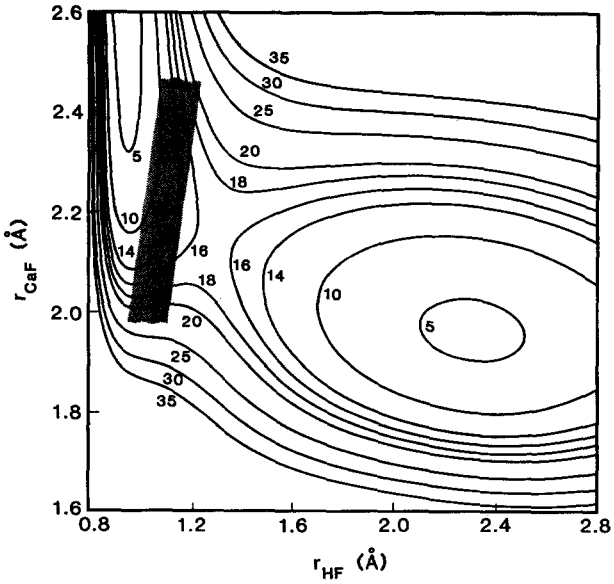

FIG. 2. Energy contours (in kcal/mol) for the Ca + HF → CaF + H potential energy surface with the Ca–F–H angle fixed at 75°. Reaction proceeds from the upper left-hand side to the lower right-hand side of the figure. The broad well in the products channel leads to formation of a stable H–Ca–F complex. The shaded area represents the range of geometries where the electron transfer occurs from Ca to H as determined by the net atomic charge on Ca varying between + 0.1 and + 0.3.

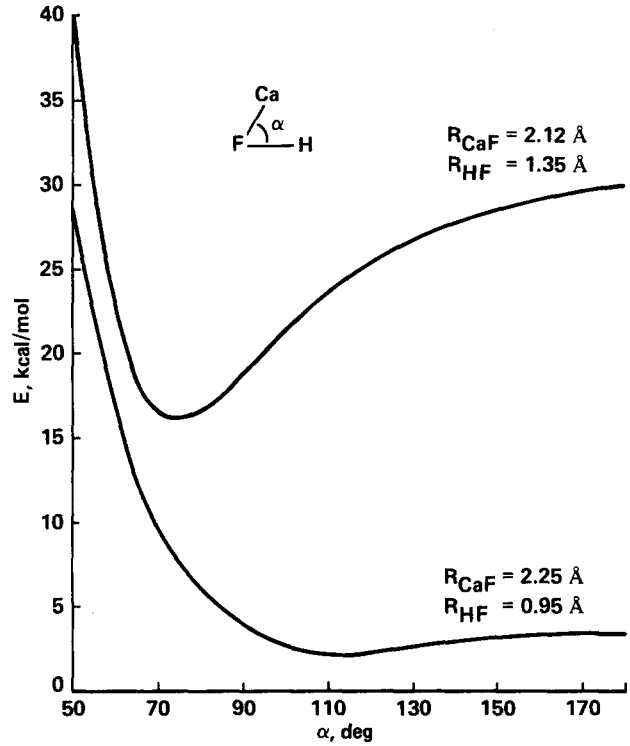

FIG. 3. Variation of Ca + HF interaction energy as a function of α, the Ca–F–H angle, with fixed Ca–F and H–F separations. The lower curve is for the entrance channel of the potential energy surface while the upper curve corresponds to the values of r_{CaF} and r_{HF} found for the 75° saddle point.

cium species. The 75° saddle point thus serves as the maximum energy on the reaction coordinate for both exchange and insertion reactions. It is also apparent that the entrance channel on this potential energy surface is extremely flat and does not contain even a shallow well. In fact, the Ca atom can approach rather close to HF without experiencing a significant increase in potential energy and without causing elongation of the HF bond. The abrupt Ca to H electron transfer described above occurs roughly within the shaded region of Fig. 2. For smaller values of r_{HF}, the colliding species resemble Ca and HF, but for larger values, they are more like CaF and H. The saddle point is clearly located in the product channel (classified as a "late barrier"). Figure 3 contains the computed Ca–F–H bending potentials for two sets of CaF and HF bond distances. The strong preference for broadside attack of Ca on HF (small angles) is clearly evident. Additionally, the abruptness of the rise in energy and energy preference can be seen. For $r_{CaF} = 2.25$ Å, the bending potential is fairly flat and the interaction energy is less that 5 kcal/mol for Ca–F–H angles between 90° and 180°. If, however, the Ca atom is moved slightly closer to the F atom (i.e., to 2.12 Å) and the HF bond is elongated, the picture changes dramatically, i.e., the interaction energy is much larger and a marked preference for even smaller Ca–F–H angles has developed. Thus, the reaction coordinate, which initially favors Ca approach to the fluorine end of HF, switches to broadside attack for smaller r_{CaF}.

A harmonic normal mode vibrational analysis was performed for the 75° saddle point region of the potential energy surface. The stretching force constants were evaluated using the cubic spline interpolation. The bending and the bend–stretch off-diagonal force constants were determined from other computed points on the surface. At the saddle point, the imaginary frequency is 1269.8 cm^{-1} and the two real frequencies are 973.8 and 397.7 cm^{-1}. These serve to reduce the effective barrier for reaction of ground vibrational state HF by nearly 4 kcal/mol to 12.2 kcal/mol. Referenced to Ca + HF($v = 0$), however, the sum of the barrier height plus the zero point vibrational energy is 0.4 kcal/mol greater than the HF ($v = 1$) vibrational energy.

The energetically stable H–Ca–F molecule is found to be linear with equilibrium bond lengths of 2.05 and 2.11 Å for CaF and CaH, respectively. Relative to Ca + HF, its equilibrium energy is − 39.0 kcal/mol. H–Ca–F has an extremely soft bending mode and can undergo large amplitude distortions with little increase in energy. The potential energy curve for bending with fixed bond lengths is shown in Fig. 4. The region around the minimum is extremely flat (bending amplitudes of ± 60° are readily achieved with very little energy change). At small H–Ca–F angles, the bending curve actually goes through a maximum due to stabilization from a nascent HF bond. The geometry at the low angle potential energy maximum is quite close to that of the Ca–F–H saddle point ($r_{CaF} = 2.10$ Å, $r_{HF} = 1.25$ Å, and Ca–F–H angle 74.8°).

Given the small error in the computed endothermicity, we believe that the potential energy surface reported herein is highly accurate. While it is not possible to place realistic error bounds on the saddle point energies or the H–Ca–F well depth, it is generally acknowledged that barrier heights determined by *ab initio* quantum chemistry methods are too large,[27–31] but that the use of extensive basis sets and electron correlation treatments can reduce the errors to 1–2 kcal/

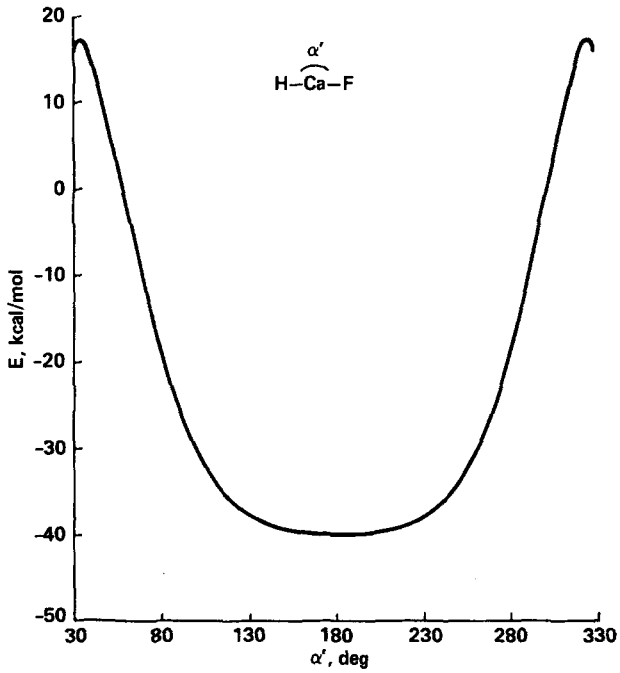

FIG. 4. Bending potential energy curve for the H–Ca–F complex with r_{CaF} and r_{CaH} fixed at their equilibrium bond lengths (2.05 and 2.11 Å, respectively).

mol. In the present study, it is likely that the 75° saddle point is 2 or 3 kcal/mol too high in energy. The presence of the H–Ca–F well in the exit channel of the 75° surface means that the experimental observation that only vibrationally excited HF molecules react does not actually place a bound on the height of the energy barrier. Insertion to form a transient complex could even occur with no activation energy, but the preference for vibrational excitation over translational energy in the reaction cross sections probably implies the existence of at least a moderate barrier in the entrance channel. If the barrier on the computed potential energy surface is too large, then our calculations would underestimate the extent of long-lived H–Ca–F complex formation. However, conclusions about product energy partitionings would not likely be affected.

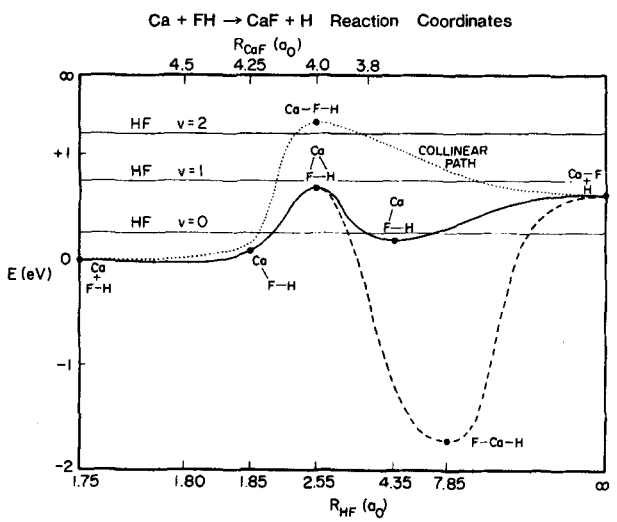

FIG. 5. Schematic representation of the potential energy profiles (in eV) along the Ca + HF → CaF + H reaction coordinates. Reaction pathways for both collinear and broadside collisions are shown. The 75° (triangular) barrier also leads to formation of the stable H–Ca–F species. For reference, the energies of low-lying HF vibrational levels are given. Note that the barrier on the nonlinear reaction path lies below HF($v = 1$).

The key features of the Ca–F–H potential energy surface are summarized in Fig. 5 which is a schematic representation of the reaction coordinates. The computed barrier to reaction is completely consistent with experiment in that it is lower in energy than Ca + HF($v = 1$). For moderate thermal collision conditions, the collinear Ca–F–H path should be energetically inaccessible. Thus, the reaction dynamics should be characterized by broadside attack of Ca on HF and the likely formation of transient H–Ca–F insertion complex structures.

III. POTENTIAL SURFACE FIT

A discussion of various techniques previously utilized for fitting *ab initio* atom–molecule potential energy surfaces has been given in Ref. 21. From this discussion and the references cited therein, it is obvious that the task of accurately fitting fully three-dimensional *ab initio* potential energy surfaces is an extremely arduous one. In general, mathematically sophisticated, deterministic procedures (e.g., three-dimensional spline fits) have met with limited success. Given the high dimensionality of the problem, coupled with effects due to chemical specificity, this situation is probably not surprising. By and large, a viable fitting procedure must be tailored both to the sort of quantum chemistry data available and to the specific nature of the surface being fit.

In common with the Be + HF system, the present Ca–F–H potential contains features (e.g., rapid switching from reactant to product properties, existence of a deep H–Ca–F potential well, etc.) which render an accurate fitting procedure especially difficult. As evidence of this fact, it might be noted that the functional fit to the *ab initio* Be + HF potential energy surface in Ref. 21 was accurate to within only a root mean square deviation of ~9 kcal/mol. This figure gives a concrete indication of the difficulty of constructing an accurate functional fit to *ab initio* alkaline earth + hydrogen halide potential energy surfaces.

In addition to configurations which correspond to isolated diatomic species (i.e., HF, CaF, and CaF), the *ab initio* calculations described above generated potential energy values for 175 Ca–F–H geometries. The majority of these were clustered about the physically more important regions of configuration space. Thus, nearly half the number of computed points, 74, corresponded to atomic configurations for which the value of the Ca–F–H angle is 75°. As discussed in the previous section, the minimum energy barrier for Ca atom attack on HF occurs at this angle. An additional 44 points corresponded to collinear atomic geometries: 29 to Ca–F–H, 5 to Ca–H–F, and 10 to H–Ca–F. The remaining 56 computed potential points were distributed over various intermediate configurations.

After consideration of several possibilities, a decision was made to fit the computed *ab initio* potential points in the form of terms containing linear combinations of powers and

products of powers of the HF, CaF, and CaH bond lengths. While totally empirical in nature, such a procedure permitted efficient use of the geometric characteristics of the *ab initio* potential points available. The terms containing linear combinations of powers and products of bond lengths were multiplied by products of the attractive portions of the appropriate asymptotic diatomic potentials. Such products, which are essentially exponential in nature introduce in an automatic fashion two essential elements: (a) due to their exponential nature, they tend to damp oscillatory behavior which may occur in the linear combination terms, and (b) as the appropriate asymptotic limit is approached, the terms in which they appear vanish. In addition, when justified by necessity and the nature of the *ab initio* data, terms appearing in the fitted potential were further modulated by switching functions and terms explicitly involving the Ca–F–H angle.

The powers and products of bond lengths utilized in the linear combination terms were determined by an iterative (but generally not convergent!) procedure, i.e., many combinations based on inspection of the *ab initio* data were tried. Eventually, as described in detail below, the procedure employed, along with a least squares determination of free parameters in the fitted potential form yielded a fitted potential energy function which is in good quantitative agreement with the *ab initio* calculations. The quality of the functional fit obtained results from a combination of the care used in selection of atomic geometries of the (relatively few) computed *ab initio* potential points, coupled with specific empirical exploitation of the characteristics of these points.

In obtaining functional fits for the potentials of the asymptotic diatomic species (i.e., HF, CaF, and CaH), the procedure utilized in Ref. 21 was followed with the provision that the resulting fits were required to reproduce the computed dissociation energies, equilibrium bond lengths, and vibrational force constants. For HF, a Morse potential was used with parameter values: $D_e = 133.06$ kcal/mol, $r_e = 0.9260$ Å, and $\beta = 2.280$ Å^{-1}. For CaF and CaH, zeroth-order potentials for the interactions of ground state atoms were represented as simple exponential repulsions of the form $A\exp(-br)$, where r is either the CaF or CaH bond length as appropriate. For CaF, parameter values for the repulsive curves were $A = 3.6199\times10^5$ kcal/mol and $b = 4.00$ Å^{-1}, and for CaH, $A = 8.9986\times10^4$ kcal/mol and $b = 3.75$ Å^{-1}. The attractive zeroth-order interactions between Ca^+ and F^- for CaF and Ca* (i.e., Ca $4s4p$) and H for CaH were represented by Morse functions shifted upward in energy by an amount E_0 which was included to account for ionization or atomic electronic excitation as appropriate. For CaF, $D_e = 184.30$ kcal/mol, $r_e = 2.006$ Å, $\beta = 0.913$ Å^{-1}, and $E_0 = 66.07$ kcal/mol, and for CaH, $D_e = 78.36$ kcal/mol, $r_e = 2.053$ Å, $\beta = 0.893$ Å^{-1}, and $E_0 = 43.76$ kcal/mol. Avoided crossings between the CaF and CaH repulsive and attractive interactions were accounted for within the context of a simple 2×2 valence bond treatment with diagonal terms as given above and off-diagonal coupling terms of the form introduced by Grice and Herschbach[51], viz., as $Cr\exp(-dr)$. For CaF, C = 41.86 kcal/

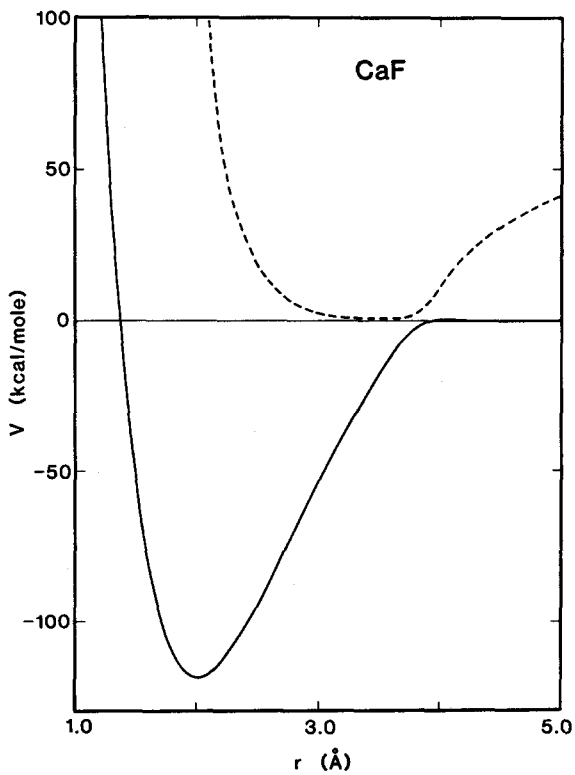

FIG. 6. CaF potential curves utilized in the fitted Ca–F–H potential energy function. As discussed in the text, dashed and solid curves result from the solution of a two configuration valence bond problem and exhibit an avoided crossing between repulsive and attractive curves. The lower solid curve reproduces the *ab initio* values of the CaF dissociation energy (to neutral atoms), equilibrium bond length, and vibrational frequency.

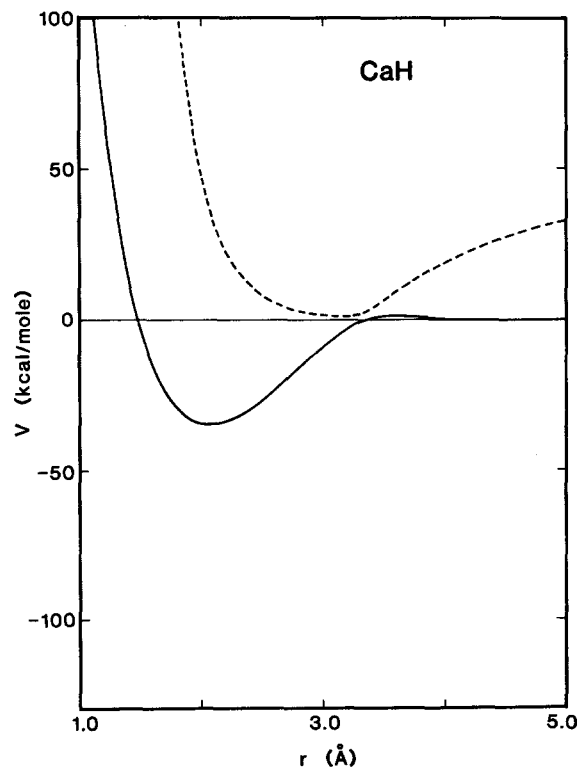

FIG. 7. Same as Fig. 6, but for CaH.

mol Å, $d = 1.50$ Å^{-1} and for CaH, C = 31.43 kcal/mol Å and $d = 1.50$ Å^{-1}. While little, if any, physical significance attaches to the individual parameter values given for CaF and CaH, their combinations lead to ground state potentials which, as noted above, reproduce the *ab initio* dissociation energies, bond lengths, and force constants. Graphical representations of the fitted diatomic CaF and CaH potential curves are presented in Figs. 6 and 7.

For the full Ca–F–H potential, the final functional form is given (with energy in kcal/mol) by Eq. (3) in which r_1, r_2, and r_3 denote, respectively, the HF, CaH, and CaF bond lengths and α is the Ca–F–H bond angle defined over the interval $(0,\pi)$. $V(r_1)$, $V(r_2)$, and $V(r_3)$ represent the HF, CaH, and CaF diatomic potentials described above and $V_{\rm att}(r_i)$ is the attractive part of $V(r_i)$.[52] With these definitions, the potential is given by

$$
\begin{aligned}
V(r_1,r_2,r_3) &= D_e(\mathrm{HF}) + 0.25\{V(r_1) + V(r_2) + V(r_3) + V_{\rm att}(r_1)[V_{\rm att}(r_3) - 33.035][P_1 + P_2 r_1 + P_3 r_3 \\
&+ P_4 r_1 r_3 + P_5 r_1^2 + P_6 r_1^3 + P_7 r_1^{-1} r_3 + P_8 r_1^{-1} r_3^2 + P_9 r_1^{-2} r_3 + P_{10} r_1^{-2} r_3^2 + P_{11} r_3^2 + P_{12} r_1^2 r_3^2] \\
&+ V_{\rm att}(r_1)[V_{\rm att}(r_2) - 21.880][P_{13} + P_{14} r_1 + P_{15} r_2 + P_{16} r_1 r_2 + P_{17} r_2^2 + P_{18} r_1^{-1} r_2^2 \\
&+ P_{19} r_1^2 + P_{20} r_1^2 r_2^2] + [1 + \tanh(a_1 r_1 + b_1)][V_{\rm att}(r_2) - 21.880] \\
&\times [V_{\rm att}(r_3) - 33.035][P_{21} + P_{22} r_2 + P_{23} r_3 + P_{24} r_2 r_3] \\
&+ 1.035\,28 \sin\alpha V_{\rm att}(r_1)[V_{\rm att}(r_3) - 33.035][P_{25} + P_{26} r_1 + P_{27} r_3 + P_{28} r_1 r_3 \\
&+ P_{29} r_1^2 + P_{30} r_3^2 + P_{31} r_1^2 r_3^2 + P_{32} r_1^3]\}\{[1 - \tanh(a_2)\exp[-\delta(\pi - \alpha)]r_1 + b_2] \\
&\times [1 - \tanh(\hat{a}_4 r_3 + b_4)]\} + 0.5\{[1 + \tanh(a_2)\exp[-\delta(\pi - \alpha)]r_1 + b_2]V(r_3) \\
&+ [1 + \tanh(\hat{a}_4 r_3 + b_4)]V(r_1)\}
\end{aligned}
\tag{3}
$$

with

$$\hat{a}_4 = 0.5[1 + \tanh(a_3\alpha + b_3)]a_4. \tag{4}$$

D_e(HF) adjusts the zero of energy to correspond to separated Ca and HF with HF at the bottom of its potential well. Values of parameters not already defined are given in Table III.

Although the functional form given Eq. (3) is complicated, it is computationally tractable in the context of a classical trajectory calculation. Further, it is a global fit that is continuous over the range[53] $0 \leqslant \alpha \leqslant \pi$ and correctly reduces to the appropriate diatomic functional form in the asymptotic limits. Examination of the fitted potential energy surface in the three body interaction region at a resolution of 0.1 Å found it to be completely free from spurious oscillatory behavior. In quantitative terms, the fitted potential form reproduces the computed *ab initio* potential points to within a root

TABLE III. Parameter values for fitted Ca + HF potential. Values are for bond distances in angstroms, and with other parameter values given in the text, produce $V(r_1,r_2,r_3)$ in units of kcal/mol.

$\delta = 0.500$	
$a_1 = 15.861\,0$	$b_1 = -46.547\,7$
$a_2 = 3.125\,0$	$b_2 = -5.750\,0$
$a_3 = 15.000\,0$	$b_3 = -17.500\,0$
$a_4 = 7.617\,0$	$b_4 = -19.830\,0$
$P_1 = 0.036\,480\,3$	$P_2 = -0.081\,940\,8$
$P_3 = 0.104\,529$	$P_4 = -0.041\,033\,2$
$P_5 = 0.052\,015\,9$	$P_6 = -0.009\,723\,36$
$P_7 = -0.070\,740\,3$	$P_8 = -0.005\,008\,32$
$P_9 = 0.010\,754\,6$	$P_{10} = 0.005\,471\,05$
$P_{11} = -0.003\,318\,05$	$P_{12} = 0.002\,427\,07$
$P_{13} = 0.014\,975\,0$	$P_{14} = -0.028\,440\,5$
$P_{15} = -0.001\,946\,32$	$P_{16} = 0.006\,394\,07$
$P_{17} = 0.004\,122\,71$	$P_{18} = -0.003\,108\,61$
$P_{19} = 0.009\,487\,18$	$P_{20} = -0.001\,727\,39$
$P_{21} = -0.002\,818\,60$	$P_{22} = 0.002\,173\,49$
$P_{23} = 0.001\,914\,11$	$P_{24} = -0.001\,395\,57$
$P_{25} = 0.010\,016\,8$	$P_{26} = -0.014\,342\,6$
$P_{27} = -0.005\,076\,84$	$P_{28} = 0.006\,946\,26$
$P_{29} = 0.000\,032\,601\,9$	$P_{30} = 0.000\,3408\,80$
$P_{31} = -0.000\,684\,213$	$P_{32} = 0.001\,783\,72$

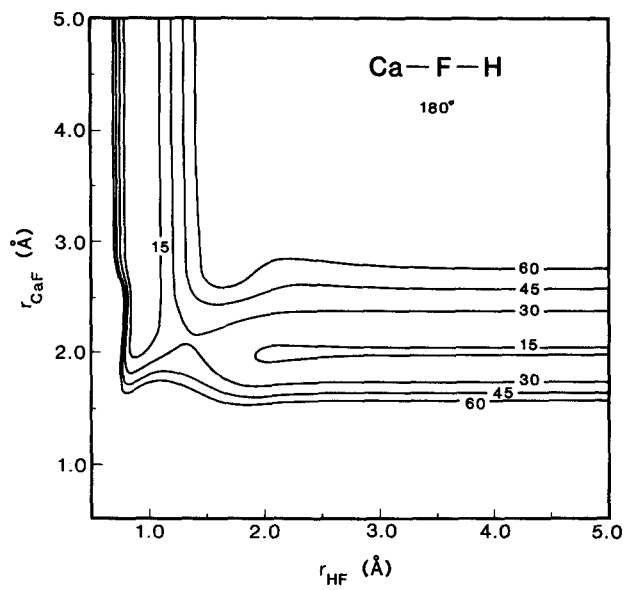

FIG. 8. Contour map of the fitted Ca–F–H potential energy function for Ca–F–H angle (α) = 180°. The value of the Ca–F–H energy (relative to separated Ca + HF) is given in kcal/mol for each equipotential contour. As in Fig. 2, Ca + HF → CaF + H reaction proceeds from the upper left-hand side to the lower right-hand side.

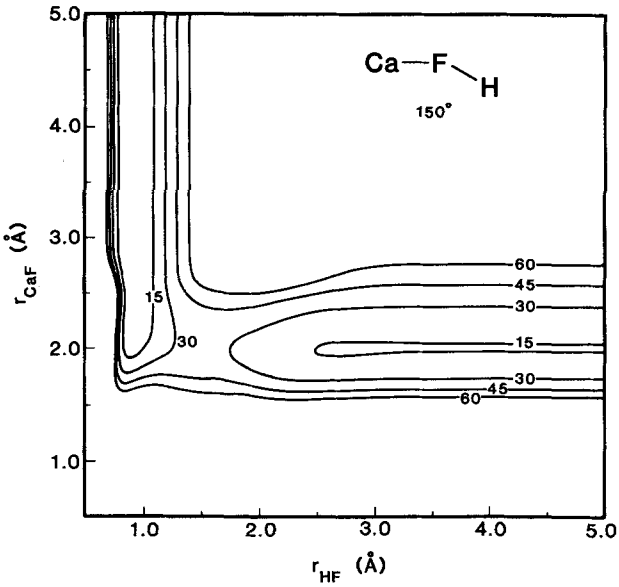

FIG. 9. Same as Fig. 8, but for $\alpha = 150°$.

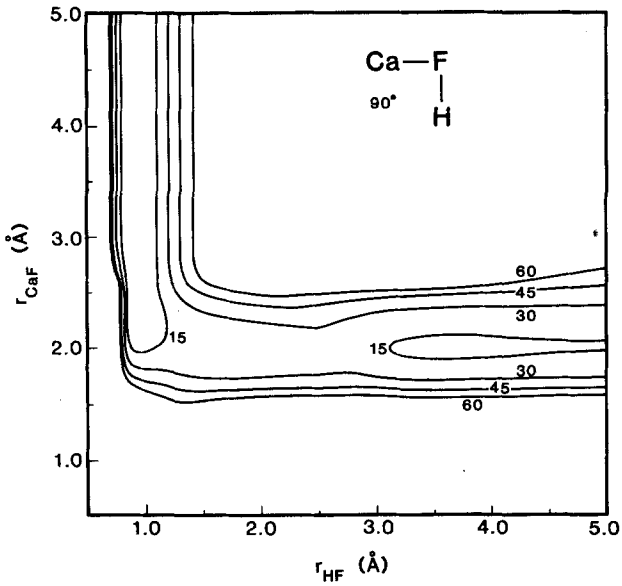

FIG. 11. Same as Fig. 8, but for $\alpha = 90°$.

mean square deviation of 1.16 kcal/mol—accuracy consistent with the bounds of chemical accuracy. Additional fitting statistics are: 89.7% of the computed *ab initio* energies are reproduced to within 2.00 kcal/mol, 95.4% to within 3.00 kcal/mol, 99.4% to within 4.00 kcal/mol, and 100% to within 4.05 kcal/mol. For points along the energetically favored Ca–F–H angle of 75°, the corresponding percentages are 94.6, 97.3, 98.7, and 100, and the root mean square deviation of these 75° fitted points is 0.96 kcal/mol. Further, fitted points with larger deviations were not clustered in any restricted identifiable region of configuration space. It should be noted that the functional fit presented here is valid only up to an energy of approximately 75 kcal/mol (relative to separated Ca + HF) which is below the CaH + F asymptotic energy. It is unlikely that any experiments in the near future will employ energies in excess of this value.

Various graphical representations of the fitted Ca–F–H potential function are presented in Figs. 8–15. As indicated in the figures, for Ca–F–H angles of 180°–120°, the potential varies relatively little. For angles of 90°–60°, the CaF + H product channel broadens as the well corresponding to H–Ca–F forms. By a Ca–F–H angle of 60°, the H–Ca–F well is quite deep. Figure 16 shows an energy contour plot for the collinear H–Ca–F complex. These contour maps illustrate the physically reasonable nature of the potential function fit.

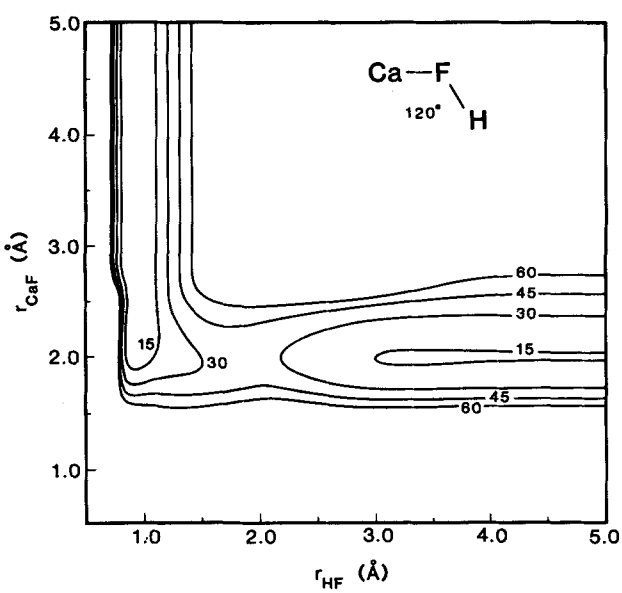

FIG. 10. Same as Fig. 8, but for $\alpha = 120°$.

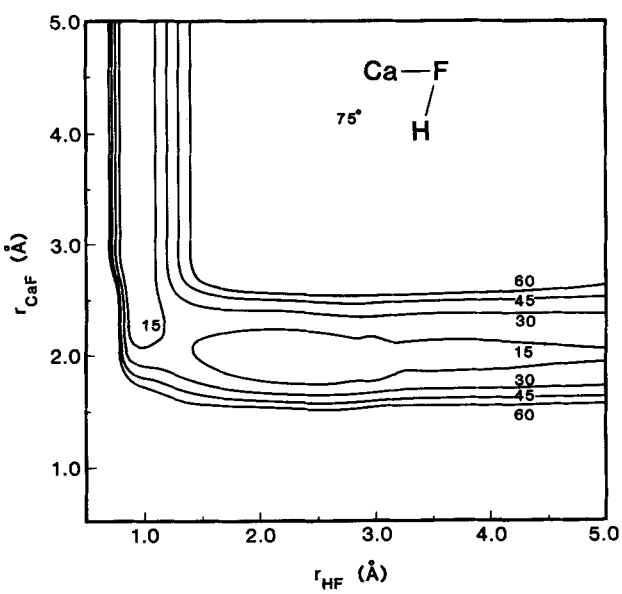

FIG. 12. Same as Fig. 8, but for $\alpha = 75°$. The beginning of a stable H–Ca–F complex is evident in the reaction exit channel. This feature is more clearly shown in the higher resolution plot of Fig. 2. For the region covered by Fig. 2, the computed and fitted potential energy contour maps are virtually identical.

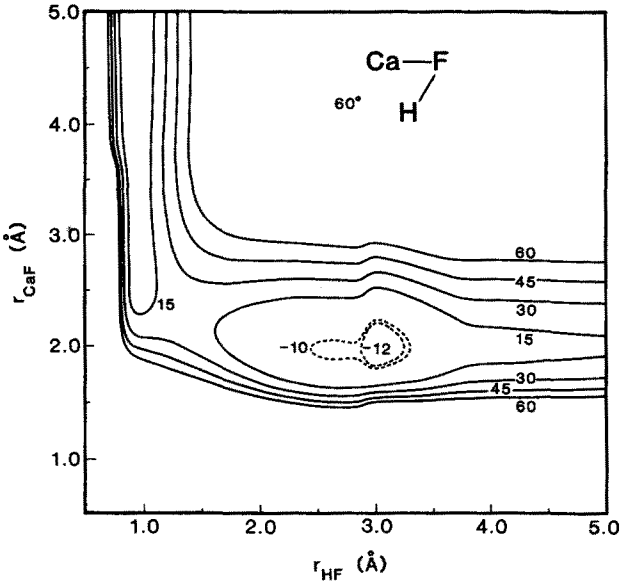

FIG. 13. Same as Fig. 8, but for $\alpha = 60°$. The potential well corresponding to H–Ca–F is now clearly visible.

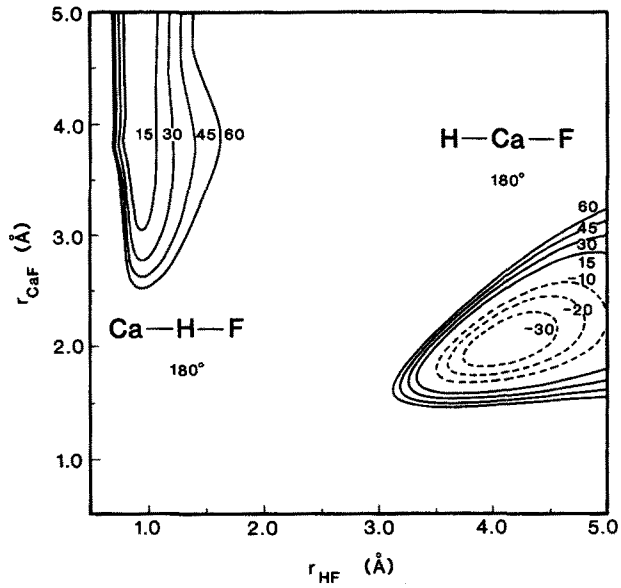

FIG. 15. Same as Fig. 8, but for $\alpha = 0°$. Separation into collinear Ca–H–F and H–Ca–F structures (both of which correspond to $\alpha = 0°$ is evident).

A higher resolution display of the fitted potential in the region of the 75° Ca–F–H energy barrier is virtually identical to that shown in Fig. 2. In fact, the saddle point on the fitted surface has an energy of 16.3 kcal/mol (0.2 kcal/mol higher than the *ab initio* result) and is located at $r_{CaF} = 2.14$ Å and $r_{HF} = 1.31$ Å (both within 0.03 Å of the bond lengths at the CASSCF-CI saddle point).

IV. TRAJECTORY CALCULATIONS AND SCATTERING RESULTS

Classical trajectory calculations utilizing the potential function given by Eqs. (3) and (4) were performed by standard techniques.[54] For integration of Hamilton's equations of motion, a sixth-order Gear hybrid integrator[55] with constant time increment was used. Since the Gear procedure is not self-starting, each trajectory was initiated by executing three cycles of a fourth order Runge–Kutta–Gill algorithm.[56] The trajectory code employed was written specifically for execution on the NASA Ames Cray XMP computer and permitted parallel integrations of up to 100 trajectories. Computations using the vectorized Cray code resulted in execution speed increases of up to an order of magnitude over those obtained with the purely scalar code. The minimum energy barrier for the Ca + HF → CaF + H reaction lies close to the energy of HF in its first excited vibrational level. Because of this, and also because existing experimental studies[1,3] have employed vibrationally excited

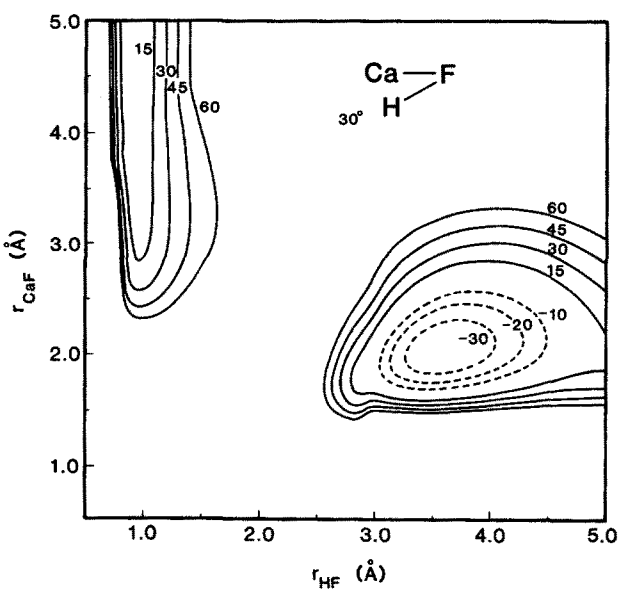

FIG. 14. Same as Fig. 8, but for $\alpha = 30°$.

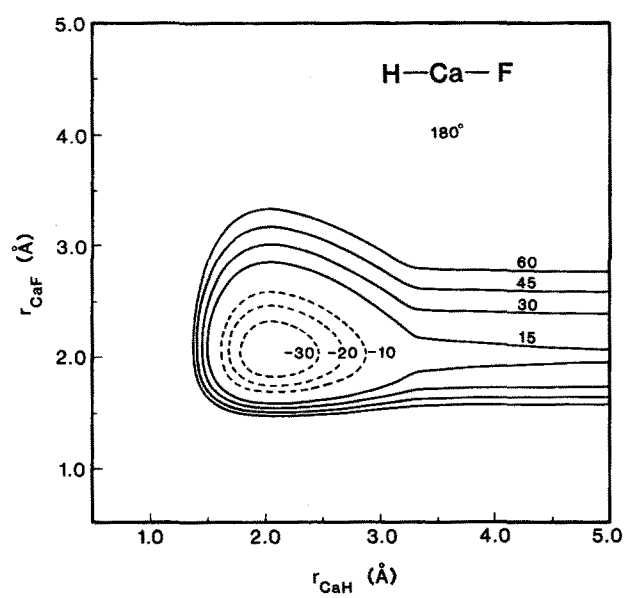

FIG. 16. Contour plot similar to Figs. 8–15 for collinear H–Ca–F.

HF, virtually all the calculations performed in the present study focused attention on the reaction of Ca with HF in various rotational levels of the $v = 1$ vibrational state. That is, the reaction

$$\mathrm{Ca} + \mathrm{HF}(v = 1,J) \rightarrow \mathrm{CaF}(v',J') + \mathrm{H} \qquad (5)$$

was studied for various Ca,HF initial relative translational energies.

Before proceeding with a description of results the obtained for the reaction of Ca with HF, a few preliminary comments are in order. As is discussed in Sec. II above and is obvious from the potential function maps presented in Sec. III, the Ca–F–H potential surface exhibits a strong preference for reaction via noncollinear attack of Ca on the HF bond axis. In quantitative terms, the energy threshold for collinear Ca–F–H reaction is ~35 kcal/mol, while for attack at a Ca–F–H angle of 75°, the corresponding barrier is less than half this value, ~15 kcal/mol. This feature is in marked contrast to the Be + HF system in which the preference for noncollinear reaction is weak.[21] Also in contrast to Be + HF, in the present case, the attacking alkaline earth atom is heavier than either atom in HF. Besides constituting interesting differences in potential surface characteristics and atomic mass combinations, these factors were found to have dramatic dynamical consequences. For example, Chapman reports that Be + HF collisions are generally simple, fast, and direct. As documented in Table III of Ref. 22, except for very high initial HF rotational states, the fraction of trajectories near the H–Be–F potential well does not exceed 15%. Even for $J = 20$, the largest fraction observed is 50%. For Ca + HF collisions, a large fraction of computed trajectories (particularly at low translational energies) were sufficiently long lived to be indicative of the formation of H–Ca–F complexes.

In performing individual trajectory integrations, time steps in the range 5.0×10^{-17} to 1.25×10^{-17} s were employed and the Ca atom was initially placed 8.0 Å from the HF center of mass. Examination of several test batches of trajectories indicated that most reactive collisions occurred for impact parameters less than 2.0 Å and as a result, a value of 2.3 Å was chosen for the maximum impact parameter in the subsequent calculations. Owing to the mass combination and the long collision times, it was not always possible to perform stable integration of the trajectories to diatomic end products. As a result, all trajectories reported were individually tested for convergence by integrating them at two or more time steps. Virtually all nonconverged trajectories exhibited excellent total energy and angular momentum conservations and were integrated to a diatomic endpoint, but they were not stable [e.g., different diatomic (v,J) and scattering angle] with respect to a decrease in integration time increment. In fact, some nonconverged trajectories even switch from nonreactive to reactive upon changing the time step. In general, the lifetimes of nonconverged trajectories were in excess of 1 to 2 ps. Since a small number of converged trajectories also had lifetimes on the order of these values, trajectory lifetime itself does not suffice to provide a totally reliable criterion for noncomplexed behavior. Because of the complicated form of the fitted potential energy function, the existence of long-lived trajectories and the necessity to test all trajectories for convergence, cost limitations placed rather severe constraints on the numbers of computed trajectories. As a result, statistical errors in computed reaction attributes are larger in many cases than might be ideally hoped for. Nonetheless, the data generated is of sufficient accuracy to support meaningful insights into the characteristics of Ca + HF collision dynamics. A similar extent of nonconverged trajectory occurrence was also observed for the test trajectories run on the modified form of the potential energy surface.[52] Finally, it should be noted that because of small values of both converged reactive and nonconverged cross sections, it was not feasible to perform calculations under conditions which exactly replicate those of existing experimental studies. Despite this, however, the computed results delineate a number of well-defined Ca + HF scattering characteristics which are subject to immediate experimental tests and, thus, suggest possibly interesting avenues for future experimental work.

Preliminary calculations established that for Ca + HF$(v = 1,J)$ scattering, initial relative translational energies of at least ~5 kcal/mol were required to produce statistically significant cross sections for converged reaction to form CaF and/or noncoverged H–Ca–F formation. Consequently, trajectory calculations were performed for collisions corresponding to relative translational energy (E_{rel}) values of 5, 10, 20, 30, and 40 kcal/mol. For the latter three values, sufficient energy to overcome the minimum barrier to reaction is initially lodged in relative translation. For $E_{\mathrm{rel}} = 5$ and 10 kcal/mol, it is necessary for initial HF internal energy to assist in surmounting the barrier. For $E_{\mathrm{rel}} = 5$, 10, and 20 kcal/mol, initial HF J values of 0, 1, 4, 7, and 10 were investigated, while for $E_{\mathrm{rel}} = 30$ and 40 kcal/mol, only $J = 1$, 4 and 7 were considered. In addition, as will be noted below, a few calculations utilizing other initial collision energies and initial HF v and J values were performed to investigate specific features of the Ca + HF reaction dynamics.

Figure 17 displays computed cross section values (in Å^2), along with their associated standard deviations, for the Ca + HF initial collision conditions cited in the previous paragraph. For each set of conditions, the smaller values correspond to cross sections for converged reactive trajectories which lead to CaF formation. The larger values represent combined cross sections for converged reaction to form CaF and nonconverged trajectories (i.e., those which correspond to long-lived H–Ca–F complex formation). In that at least a fraction of the nonconverged trajectories ultimately produce CaF + H the two values presented provide lower and upper bounds for the actual reactive cross section. For all initial translational energies studied, both sets of cross section curves are remarkably linear with respect to increasing initial HF rotational quantum number. In each frame of the figure, the solid lines represent weighted linear least squares fits[57] to the J dependences of the cross section values. It is interesting to note that at high translational energies, i.e., $E_{\mathrm{rel}} = 30$ and 40 kcal/mol, the two sets of cross section curves parallel each other, indicating that the extent of nonconverged H–Ca–F formation is insensitive to the initial HF rotational state. In contrast, as E_{rel} is lowered, the fraction of

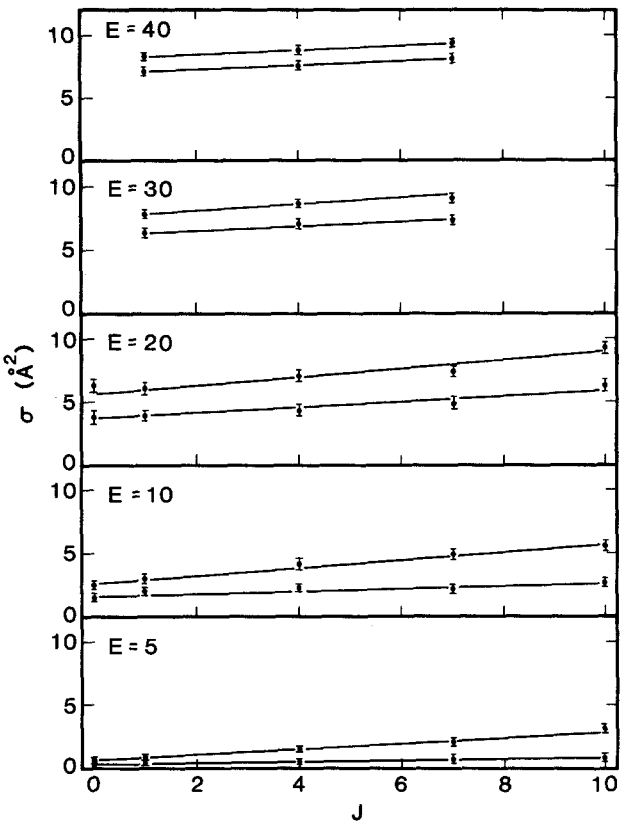

FIG. 17. Cross section values obtained for various Ca,HF initial relative translational energies and initial HF rotational states for HF($v = 1$). The value of the initial relative translational energy is noted as E in each frame. For each frame, lower curves refer to cross sections for converged CaF formation. Upper curves give the sums of cross sections for converged CaF formation and nonconverged H–Ca–F formation. For each type of cross section, the solid lines are weighted linear least squares fits to the J dependence. Bars on each point represent plus and minus one standard deviation ranges.

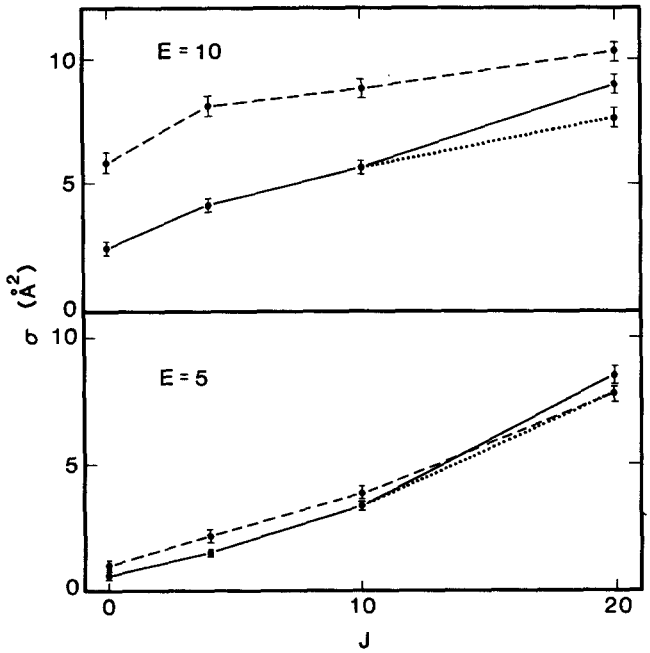

FIG. 18. Comparative plots for initial Ca,HF relative translational energies of 5 and 10 kcal/mol. For each frame, the solid lines connect cross section values for combined converged CaF and nonconverged H–Ca–F formation. Dashed lines connect cross section values for trajectories which sample the H–Ca–F potential energy well. The values connected by dotted lines are the same as those connected by solid lines minus the cross section for direct reaction (without entering the H–Ca–F well). As discussed in the text, a trajectory is said to enter the H–Ca–F well if it attains a potential energy of − 3.0 kcal/mol at some time in its evolution. Bars on each point represent plus and minus one standard deviation ranges.

nonconverged trajectories increases with increasing HF J value. Additional calculations at $E_{rel} = 5$ and 10 kcal/mol and $J = 20$ indicate that this trend does not persist beyond $J = 10$.

Insight into the role played by the H–Ca–F potential well in the dynamics of Ca + HF collisions is provided in Fig. 18 which presents comparative cross section values at $E_{rel} = 5$ and 10 kcal/mol for HF ($J = 0$, 4, 10, and 20). The solid curves in each frame connect (as in Fig. 17), cross section values for combined nonconverged H–Ca–F formation and converged reaction to form CaF. The dashed curves connect cross section values for trajectories which enter the H–Ca–F potential well. For purposes of defining this latter category of events, a trajectory was deemed to have entered the potential well if at any time the potential energy attained value of less than − 3.0 kcal/mol (relative to separated Ca + HF). As the solid curves in Fig. 18 indicate, the extent of complex formation and converged reaction to form CaF continue to increase beyond the initial HF $J = 10$ cutoff value utilized in Fig. 17. Also apparent from Fig. 18 is that at $E_{rel} = 5$ kcal/mol there is essentially a quantitative correspondence between cross section values for entering the H–Ca–F well and the sums of cross sections for nonconverged H–Ca–F formation plus those for converged reaction. For this collision energy, only at $J = 20$ did any reaction occur by trajectories which did not enter the potential well. About 2% of the total sample (corresponding to about 5% of the cross section for entering the well) underwent direct reaction. At the higher collision energy $E_{rel} = 10$ kcal/mol, cross section values for entering the well are consistently larger than the sum of those for complex formation and converged reaction. This behavior indicates that at higher energies a significant fraction of transient complexes (often up to 50%) dissociate back to reactants. As was the case for $E_{rel} = 5$ kcal/mol, no trajectories, were observed to react without entering the potential well for $J \leqslant 10$. At $J = 20$ about 7% of the total number of trajectories corresponded to direct reactive collisions without forming H–Ca–F.

Characteristics of energy disposal in converged reactive trajectories of the type denoted in Eq. (5) are displayed in Figs. 19–21. In Fig. 19, for all E_{rel} values studied, the fractions of available product energy entering relative CaF, H translation, CaF vibration, and CaF rotation ($\langle f_T \rangle$, $\langle f_V \rangle$, and $\langle f_R \rangle$, respectively) are plotted as functions of the initial HF rotational state. The obvious constancy of the product fractional energy partitionings with respect to both E_{rel} and J constitutes the most dramatic feature of the results. The one slight variation from this constancy is provided by $E_{rel} = 5$ kcal/mol, for which (as a function of J) $\langle f_V \rangle$ is generally larger and $\langle f_R \rangle$ is generally smaller than corresponding values for larger collision energies.

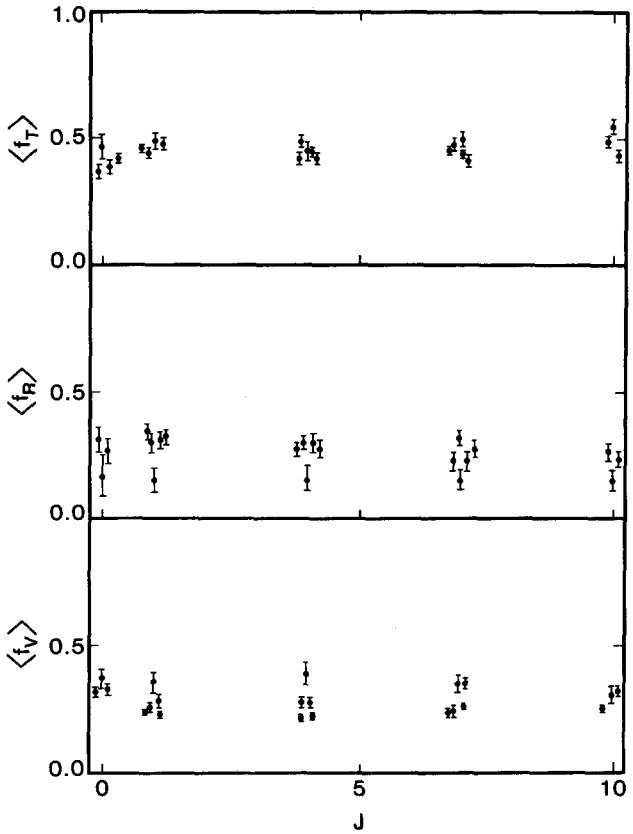

FIG. 19. Fractional product energy disposals for converged, reactive trajectories. Values of $\langle f_T \rangle$, $\langle f_V \rangle$, and $\langle f_R \rangle$ are shown for all relative translational energies and HF J values up to $J = 10$ for which calculations were performed. For all J values, the $E_{rel} = 5$ kcal/mol $\langle f_V \rangle$ values are consistently slightly larger and $\langle f_R \rangle$ values are consistently slightly smaller than those for larger E_{rel}'s. For clarity, values corresponding to common J values have in some cases been offset slightly horizontally. Bars on each point represent plus and minus one standard deviation ranges.

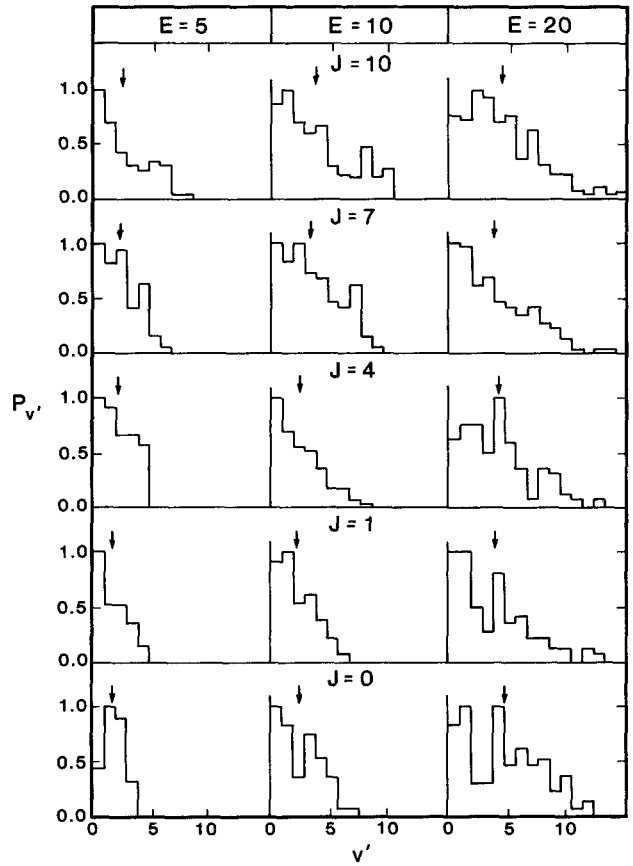

FIG. 20. Histogrammic vibrational distributions for converged CaF formation. E_{rel} values are given (in kcal/mol) as E at the top of each column of frames and the initial HF J value is given in the center frame of each row. Arrows in each frame locate the CaF v' value corresponding to the mean of the histogrammic distribution.

For completeness, histogrammic CaF product vibrational and rotational distributions, again resulting from converged reactive trajectories and for $E_{rel} = 5,10$, and 20 kcal/mol are presented in Figs. 20 and 21. In each frame, the arrow identifies the value of v' or J' (as appropriate) which corresponds to the mean of the distribution. For given E_{rel}, the product vibrational distributions shown in Fig. 20 broaden somewhat with increasing HF rotational state. However, the mean v' values remain constant. Similar behavior is evident in the CaF rotational distributions which are presented in Fig. 21.

Figure 22 presents cross section data from a limited study designed to evaluate the effects of partitioning of initial reactant energy. For cases with HF initially in rotational state $J = 0$, 4 or 10, collisions with HF($v = 0$), HF($v = 1$), and HF($v = 2$) were studied. For each J value, the total collision energy (relative translational plus HF internal) was adjusted to match the value used for $E_{rel} = 20$ kcal/mol and HF($v = 1$). As in Fig. 17, in each frame of Fig. 22, the lower curve corresponds to cross section values for converged formation of CaF while the upper curve corresponds to the sum of complex formation and converged CaF formation. It is apparent from Fig. 22 that going from HF($v = 0$) to HF($v = 1$) at constant total energy produces a dramatic increase in cross section. Further excitation of HF vibration, however, produces virtually no effect. Such behavior is not surprising in view of the fact that, as noted above, the vibrational energy of HF($v = 1$) lies very close to the minimum energy barrier for Ca + HF reaction.

Finally, Fig. 23 presents an abbreviated study of the effect of initial HF angular momentum alignment on Ca + HF reactivity. Such orientation effects have been noted in experimental studies of Sr + HF reactive scattering.[3] The cases chosen for study here were Ca + HF($v = 1, J = 4$) at E_{rel} values of 5, 10, and 20 kcal/mol. The upper two curves in the figure represent cross sections for combined complex formation and converged reaction, while the lower two curves correspond to cross sections for converged formation of CaF only. For the solid curves, the HF angular momentum vector is initially aligned perpendicular to the Ca,HF relative velocity vector, while for the dashed curves, the initial alignment is parallel. It is evident, particularly for the higher collision energies, the HF alignment produces a dramatic effect on reactive cross section. Owing to statistical uncertainties in the computed product energy partitionings, the computed results do not allow any definite conclusions relevant to the effects of reagent angular momentum alignment on CaF product energy disposal. Since the experimental Sr + HF studies document

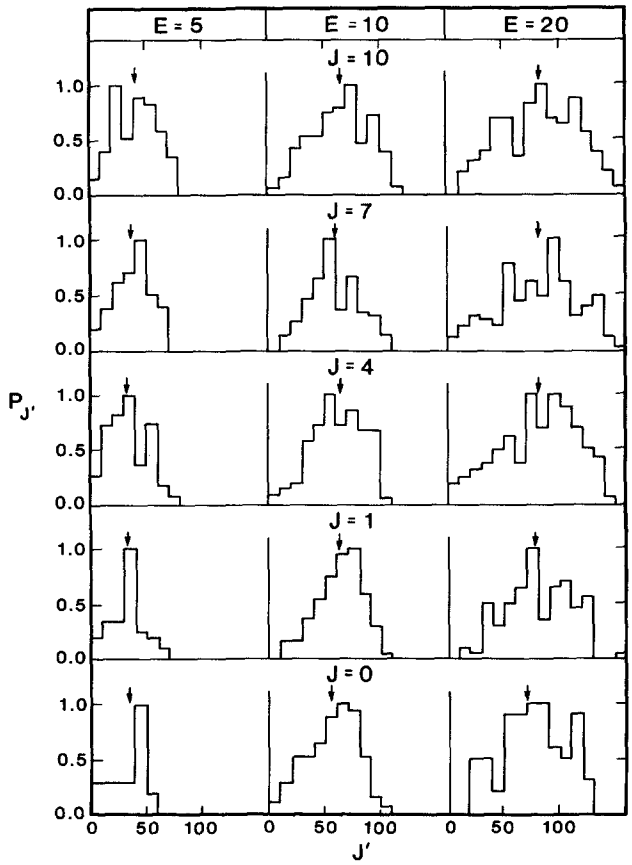

FIG. 21. Similar to Fig. 20, but for converged CaF rotational distributions.

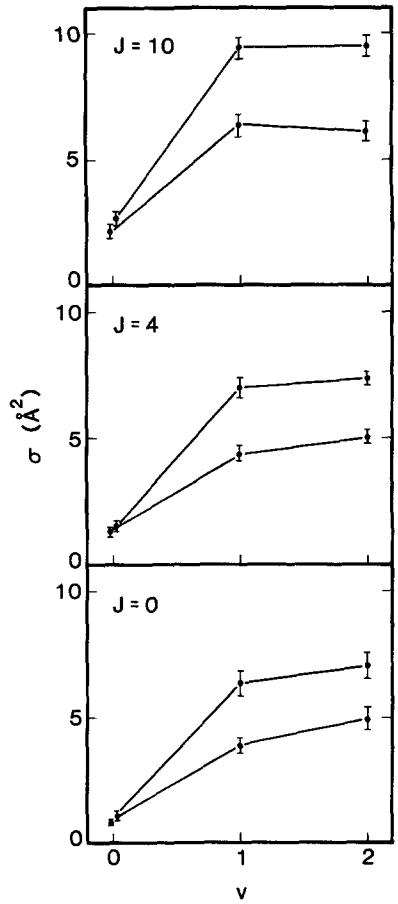

FIG. 22. Cross section plots for various HF v and J values at constant total energy. The HF J value is identified in each frame. For each frame, the lower curves give cross section values for converged CaF formation while the upper curves give cross section values for combined converged CaF and nonconverged H–Ca–F formation. Bars on each point represent plus and minus one standard deviation ranges.

an observable effect of reagent alignment on product energy disposal, further studies which investigate this point are in progress.[58]

V. DISCUSSION

The averaged collision data presented in the previous section support a number of generalizations concerning the detailed dynamics of Ca + HF reactivity.

For each set of collision conditions investigated, the fraction of nonconverged trajectories is large. This fact is demonstrated by differences between the sets of curves in individual frames of Fig. 17. In general, nonconverged trajectories are indicative of long-lived H–Ca–F complexes. The large numbers nonconverged events observed suggests that in contrast to Be + HF, for Ca + HF, the H–Ca–F potential well is readily accessible dynamically. At low values of E_{rel} (i.e., 5 and 10 kcal/mol), the importance of sampling the potential well is documented by the dashed curves in Fig. 18 and, as a result of this behavior, the Ca + HF reaction can be described as proceeding through a mechanism in which the Ca atom inserts into the H–F bond. However, unlike other insertion reactions that have been subjected to experimental and theoretical study [such as $O(^1D) + H_2$ [59–62]], the existence of a significant energy barrier in the entrance channel further complicates the reaction dynamics.

The importance of the Ca insertion pathway and the existence of significant numbers of collisions involving long-lived H–Ca–F complex formation is something of a mixed blessing. On the one hand, such behavior provides a fascinating example of an interesting type of chemical behavior. On the other hand, however, simple intuitive mechanical explanations of observed scattering results tend to be obscured.

From Fig. 18, it is apparent that for fixed, low translational energies, the cross sections for sampling the potential well increase with increasing value of the initial HF rotational quantum number J. A plausible explanation for this result is that at constant E_{rel}, a fairly slow moving heavy Ca atom approaching a rapidly rotating HF molecule is presented more opportunities to line up close to the favored 75° Ca–F–H configuration and thus, is more likely to enter the H–Ca–F potential well. Cross section values both for converged CaF formation and for nonconverged H–Ca–F formation show marked energy dependences. From the lower curves in each frame of Fig. 17, it is clear that at fixed E_{rel}, the cross section for converged reaction to form CaF increases with increasing J value. At the higher values of E_{rel} (i.e., 30 and 40 kcal/mol), the cross section for nonconverged H–Ca–F formation (given by the difference between the upper and lower curves in each frame of Fig. 17) is nearly independent of J, while for E_{rel} values of 20 kcal/mol and below, this quantity increases with increasing J value. At E_{rel} = 5 kcal/

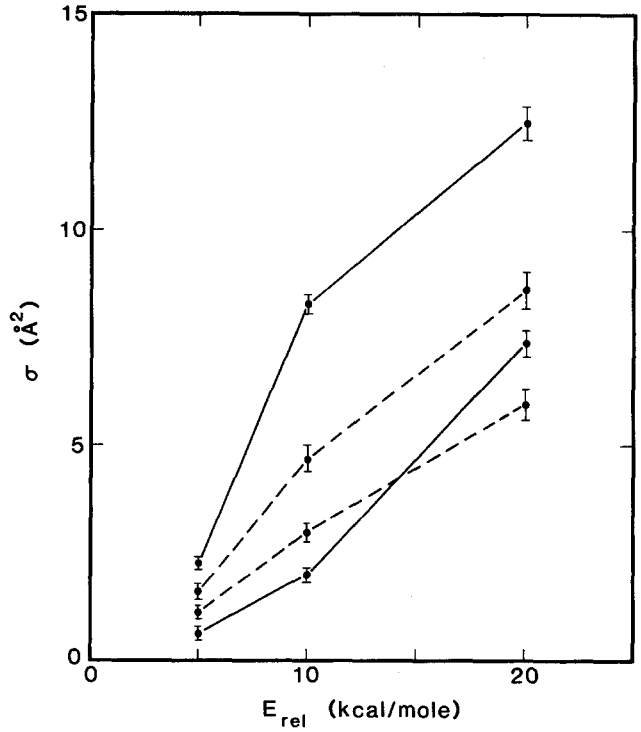

FIG. 23. Effect of initial HF angular momentum vector alignment on Ca + HF reactivity. The lower two curves give cross section values for converged CaF formation and the upper two curves give cross section values for combined converged CaF and nonconverged H–Ca–F formation. For each set of cross sections, for solid curves, the initial HF angular momentum vector is initially aligned perpendicular to the initial Ca,HF relative velocity vector. For dashed curves, the alignment is parallel. Bars on each point represent plus and minus one standard deviation ranges.

mol, the lowest value of E_{rel} considered, Fig. 18 demonstrates that the number of trajectories sampling the H–Ca–F well corresponds very closely to the total number of trajectories which either form converged CaF or nonconverged H–Ca–F. This fact, combined with the increasing cross section for converged CaF formation apparent in Fig. 17 thus indicates that, at least at low values of E_{rel}, increasing HF rotational energy is effective in promoting escape from the potential well to form CaF. This interpretation is bolstered by the fact that at $E_{rel} = 5$ kcal/mol and $J = 20$ (not shown in Fig. 17), the cross sections for converged CaF and nonconverged H–Ca–F formation are equal. Similar cross section behavior is exhibited by collisions at $E_{rel} = 10$ kcal/mol and $J = 20$.

A translational energy effect on cross sections is also apparent from Fig. 18. As already noted, for $E_{rel} = 5$ kcal/mol, there exists a virtually quantitative correspondence between potential well sampling and either reaction to form CaF or long-lived H–Ca–F. In the upper frame of the figure (i.e., at $E_{rel} = 10$ kcal/mol), the cross section for well sampling is consistently larger (often by a factor of about 2) than the combined cross section for CaF and H–Ca–F formation. This behavior clearly indicates that a large fraction of trajectories which sample the well ultimately return in a converged fashion to form reactants.

That the behaviors described above are not merely manifestations of total energy effects is clear from examination of cross section values for $E_{rel} = 5$ kcal/mol, $J = 10$ and $E_{rel} = 10$ kcal/mol, $J = 0$. These sets of collision conditions correspond to nearly the same total energy, yet Figs. 17 and 18 reveal no similarities in cross section behavior between them. Further evidence for specificity of energy effects (i.e., promotion of converged CaF formation by increasing HF rotation and promotion of converged return to reactants by increasing relative Ca,HF translational energy) is provided by the upper frame of Fig. 18 and the $E_{rel} = 10$ kcal/mol frame of Fig. 17. Over the range $J = 0$–10, cross section values for (a) potential well sampling, (b) combined converged CaF and nonconverged H–Ca–F formation, and (c) converged CaF formation all increase with increasing J value. However, as is clear from Fig. 18, at $J = 20$, the cross sections for (a) and (b) tend to coalesce indicating that converged CaF product formation is enhanced by increasing HF rotation. The opening of the direct reaction channel (i.e., reactive collisions which do not sample the potential well) is partially responsible for this result.

Despite the marked differences in the energy dependences of cross section values for potential well sampling, long-lived complex formation and converged CaF formation, fractional product energy disposals obtained from converged, reactive trajectories are remarkably insensitive to variations in both E_{rel} and J. This behavior, which is probably one of the more remarkable results obtained in the study, is apparent in Fig. 19 where, with the possible exception of $E_{rel} = 5$ kcal/mol, the fractions of available product energy entering CaF vibration, CaF rotation, and CaF, H relative translation are seen to be essentially identical (as has been noted previously, for $E_{rel} = 5$ kcal/mol, compared to other E_{rel} values, $\langle f_V \rangle$ values are consistently slightly larger and $\langle f_R \rangle$ values are consistently somewhat smaller.). Since, particularly at low collision energies, sizable fractions of converged reactive trajectories sample the potential well, the insensitivity of product energy disposal to E_{rel} and J (and, thus to the total collision energy) would seem to indicate this reaction occurs before energy randomization in the H–Ca–F complex occurs. Thus, in effect, the H–Ca–F structures may be non-RRKM in a classical sense.

The insensitivity of CaF product attributes to collision conditions is illustrated in absolute (as opposed to fractional) terms in Figs. 20 and 21. It is interesting to note that at the lowest E_{rel} value (i.e., 5 kcal/mol), the computed vibrational distributions are qualitatively similar to those obtained in low energy Ca + HF scattering experiments,[1,3] the results of which are in general accord with phase space theory. Thus, while exhibiting classical non-RRKM behavior, converged trajectories at low E_{rel} which lead to CaF formation may nonetheless be statistical in the sense of phase space theory.

Beyond E_{rel} and J effects of Ca + HF reactivity and energy disposal, results presented in Fig. 22 clarify the role played by HF vibrational excitation. As noted in the previous section, at constant total energy, excitation of HF to the $v = 1$ level greatly increases the cross sections for converged CaF formation as well as those for combined converged CaF formation and long-lived complex formation. Beyond $v = 1$, little if any, effect on reactivity is obtained

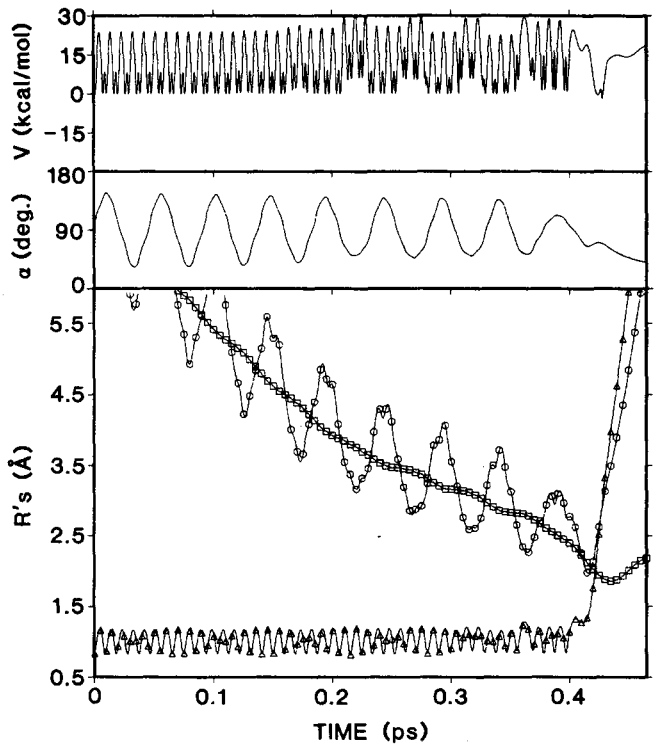

FIG. 24. Time evolution of r_{CaF}, r_{CaH}, and r_{HF}, symbols □, ○, and △, respectively, and Ca–F–H angle (α) and potential energy (V) for a converged reactive trajectory Ca + HF($v = 1, J = 20$) → CaF($v' = 2.7, J' = 44.8$) + H at $E_{rel} = 5$ kcal/mol.

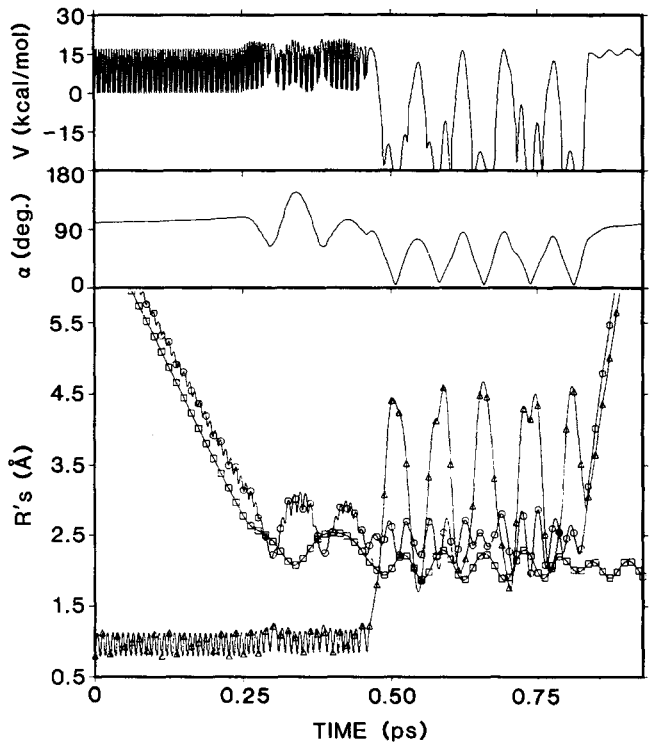

FIG. 26. Same as Fig. 24, but for the reaction Ca + HF($v = 1, J = 0$) → CaF($v' = 1.0, J' = 41.9$) + H with $E_{rel} = 5$ kcal/mol.

with further vibrational excitation. The vibrational enhancement observed for both sets of cross sections appears to be greater than the enhancement due to increased E_{rel} noted earlier. Thus, the effect of increasing energy on reactivity appears to follow the order vibration > translation > rotation.

Finally, from Fig. 23, for Ca + HF it is apparent that in contrast to results obtained [22] for Be + HF, the initial alignment of the HF angular momentum vector produces a

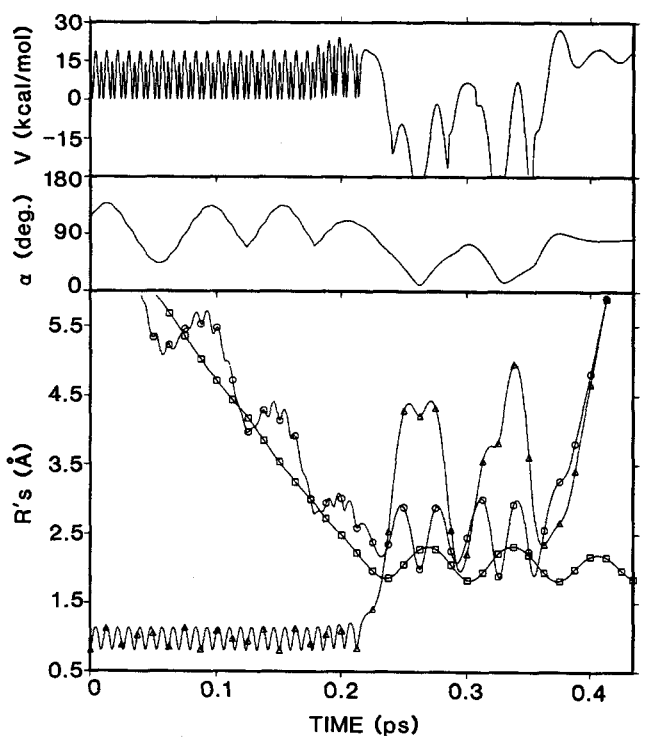

FIG. 25. Same as Fig. 24, but for the reaction Ca + HF($v = 1, J = 10$) → CaF($v' = 2.7, J' = 19.4$) + H with $E_{rel} = 10$ kcal/mol.

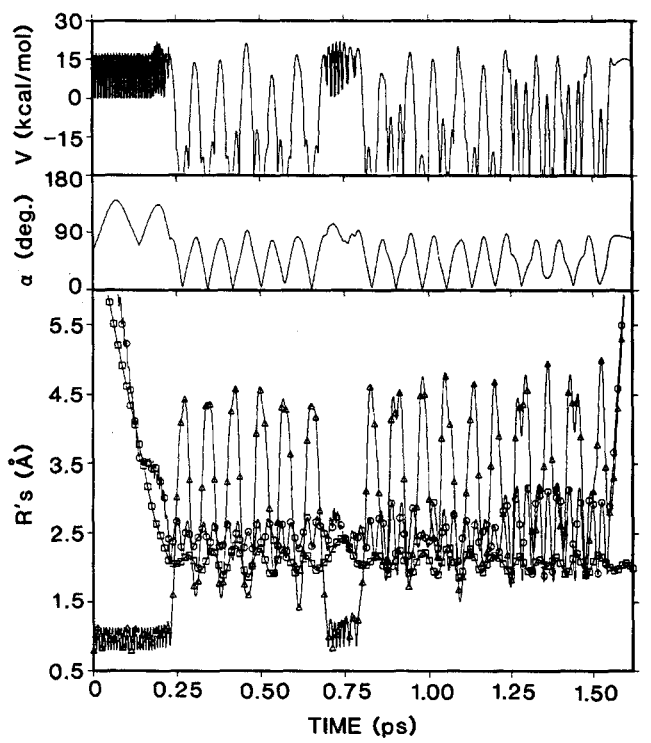

FIG. 27. Same as Fig. 24, but for the reaction Ca + HF($v = 1, J = 4$) → CaF($v' = -0.2, J' = 69.2$) + H with $E_{rel} = 10$ kcal/mol.

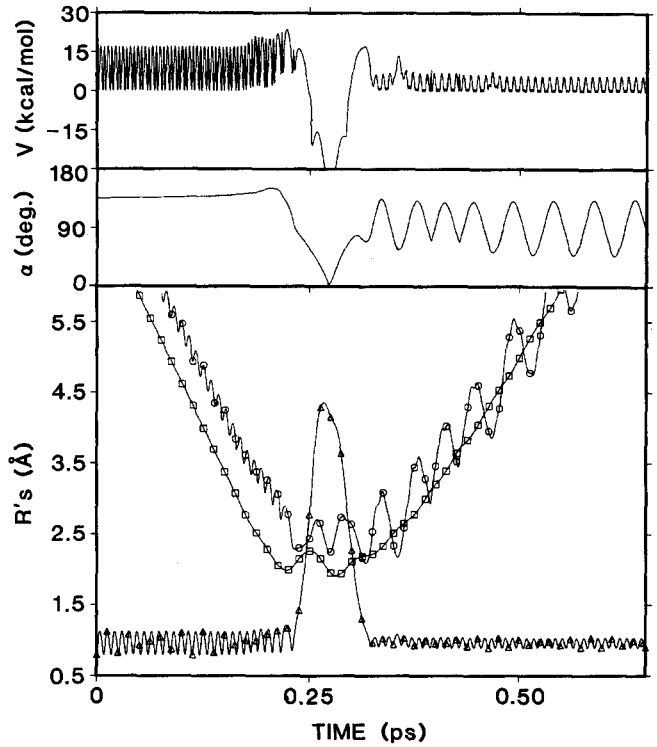

FIG. 28. Time evolution of a converged nonreactive trajectory. Symbols have the same meanings as in Fig. 24. $E_{rel} = 10$ kcal/mol. Trajectory started with HF($v = 1, J = 0$) and ended with HF($v' = -0.2, J' = 17.3$). The final scattering angle (defined between initial and final Ca to HF center-of-mass velocity vectors) is 137.6°.

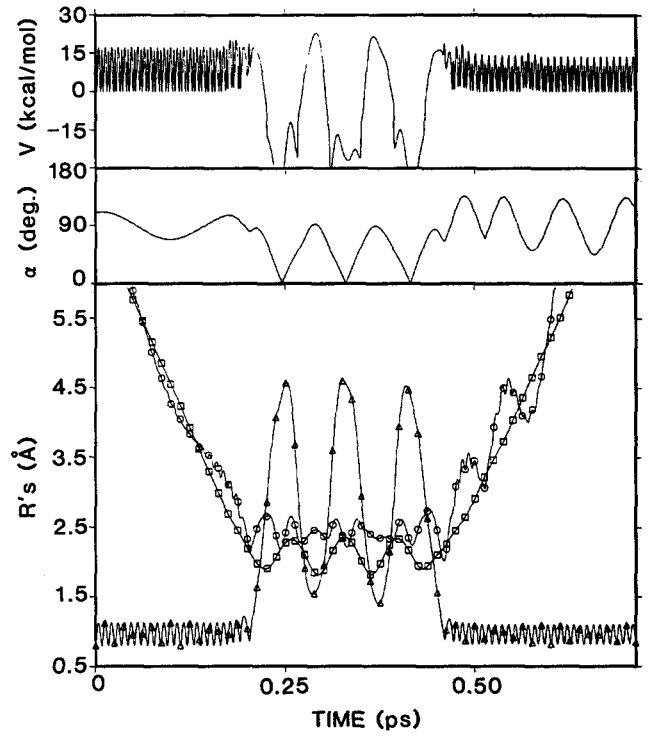

FIG. 29. Same as Fig. 28, but starting with HF($v = 1, J = 4$) and ending with HF($v' = 0.6, J' = 9.8$). $E_{rel} = 10$ kcal/mol and the scattering angle is 30.8°.

marked effect on Ca + HF reactivity. As already noted, studies in progress will hopefully clarify the origin of this effect.

Beyond the analysis of averaged reaction properties resulting from an ensemble of trajectories, it is often instructive to examine in detail the dynamical features of selected collisions. Although, of course, no individual trajectory is truly representative of an ensemble, carefully selected trajectories which reveal representative dynamical behavior can materially enhance understanding of the averaged dynamical reation attributes. Due to the existence of significant numbers of long-lived, nonconverged trajectories in the present work, selection of representative trajectories is particularly difficult. Nonetheless, progress in this direction is possible.

Plots showing the time evolutions of the three interatomic distances, the Ca–F–H angle, and the potential energy (referenced to Ca + HF) during the course of selected trajectories are shown in Figs. 24–31. Over 100 individual trajectories were examined and all the observations discussed below were seen for at least three or four different trajectories. For this reason, it is felt that the selected trajectories are representative of fairly common behavior. In the figures, a linear H–Ca–F complex would have a Ca–F–H angle of 0°, while highly bent complexes can attain a limiting Ca–F–H angle of around 90°.

Typical short-lived reactive collisions are depicted in Figs. 24–26. In all trajectories examined, the reactants were aligned with a Ca–F–H bond angle in the range of 60° to 90° when either direct reaction or complex formation occurred. For low E_{rel} and high J value, about 2% of the collisions resulted in reaction without sampling the H–Ca–F well. Such a trajectory is shown in Fig. 24. The rapid HF vibration

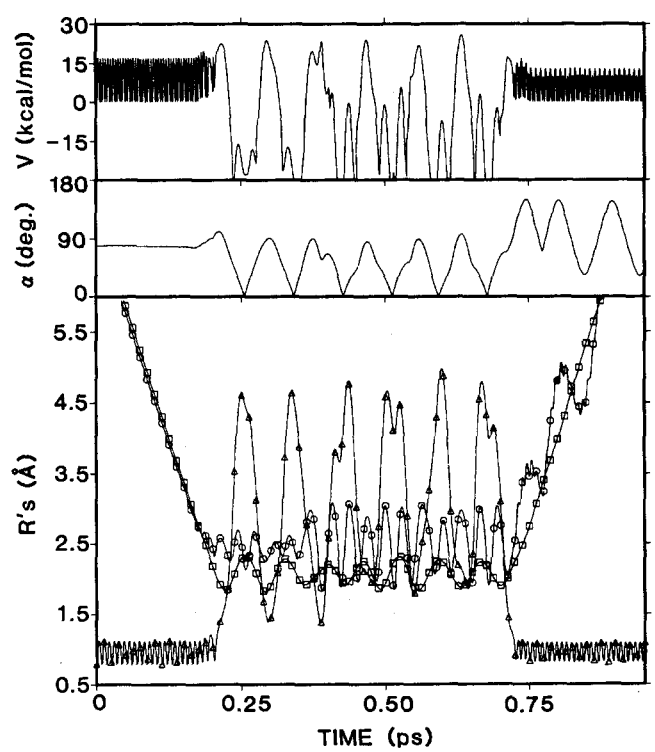

FIG. 30. Same as Fig. 28, but starting with HF($v = 1, J = 0$) and ending with HF($v' = 0.5, J' = 0.3$). $E_{rel} = 10$ kcal/mol and the scattering angle is 57.3°.

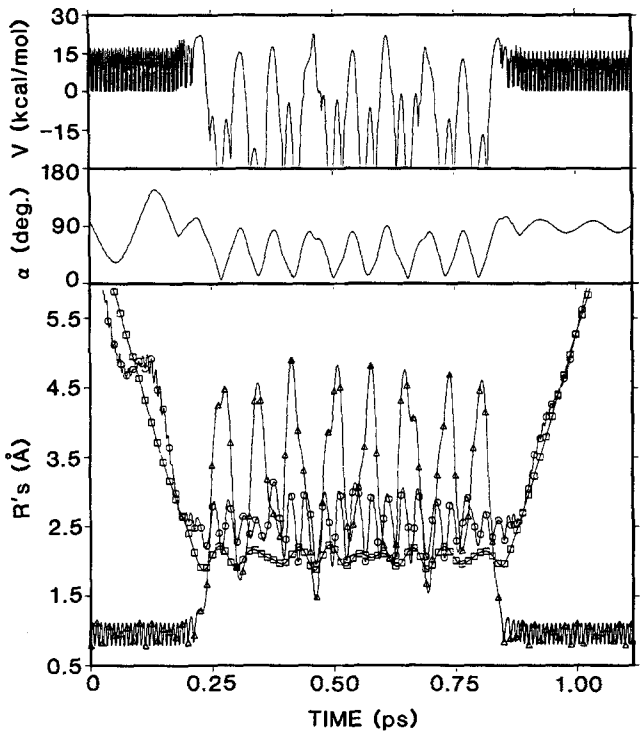

FIG. 31. Same as Fig. 28, but starting with HF($v = 1, J = 4$) and ending with HF($v' = 0.8, J' = 8.3$). $E_{rel} = 10$ kcal/mol and the scattering angle is 99.7°.

is evident in the oscillatory nature of both r_{HF} and the potential energy V. The larger amplitude oscillation of r_{CaH} and the Ca–F–H angle arise from the rapid rotational motion of the HF molecule. The Ca–F separation, however, steadily decreases, a consequence of the fact that the HF molecule rotates and vibrates about its center of mass which nearly coincides with the F atom. Once the Ca and F atoms have approached to within about 2 Å, the CaF bond forms, releasing the H atom which rapidly departs. A more common variety of reactive trajectory is given in Fig. 25. After traversing the energy barrier, the Ca inserts into the HF bond, thereby falling into the H–Ca–F well as evidenced by the sharp drop in potential energy and large excursions in r_{HF}. In the example shown, the complex undergoes one very large amplitude bending vibration during which it twice passes through near-collinear geometries (as evidenced by the large maxima in r_{HF} and near zero in α) and then abruptly ejects the H atom. Owing to vibrational angular momentum associated with the bending motion, the complex need not pass exactly through a H–Ca–F angle of 180° (i.e., $\alpha = 0°$). Concurrently, the complex undergoes two Ca–F vibrations and four Ca–H vibrations. Judging by the near constancy of the Ca–F and the Ca–H outer turning points, there is little energy exchanged among the three vibrational modes. For this class of reactive trajectories (which comprise the bulk of the observed converged trajectories which form CaF), the H–Ca–F complex undergoes one to three complete bending oscillations before breaking up. A second example of reaction after complex formation is given in Fig. 26. In this case, as the reagents approach, HF rotation is induced and the Ca and HF sit at close range until the Ca–F–H angle and the HF vibrational phase are favorable for Ca insertion to occur. This behavior undoubtedly results from the heavy + heavy–light mass combination: the Ca and F atom move rather slowly while the H atom moves rapidly, thus allowing the trajectory to sample a large range of atomic geometries while the heavy atoms are nearly frozen at a favorable separation. In this example, there again is not much intermode energy exchange during the 0.3 ps complex lifetime and the H atom seems to be abruptly and rapidly expelled.

A long-lived (1.5 ps) converged reactive trajectory is shown in Fig. 27. The most notable feature of this example is that midway through the collision, the HF molecule reforms long enough to undergo eight vibrations and one rotational period. The Ca atom, however, does not leave and ultimately reinserts. After five additional large amplitude H–Ca–F bending vibrations (during which some energy transfer between Ca–F and Ca–H vibrations occurs), the complex breaks up forming CaF + H. To a large degree, the vibrational history of this long-lived complex is not different from that observed for shorter-lived ones.

While most of the nonreactive trajectories examined do not enter the H–Ca–F well, there were at least a few exceptions for every set of initial collision conditions examined. Several of these trajectories are depicted in Figs. 28–31. In the simplest example of this phenomenon, Fig. 28, the Ca atom essentially passes through the HF bond with the reactant diatomic reforming behind it. The picture is not quite so simple, however, in that the HF molecule is left in a highly excited rotational state ($J' = 17$) and the Ca atom is backward scattered (atomic scattering angle = 138°). This behavior is equivalent to half a triatomic H–Ca–F complex bending vibration. Other trajectories were observed with 1, 1.5, and 2 complex bending vibrations. An example with 1.5 is presented in Fig. 29: the Ca approaches broadside, inserts, and oscillates back and forth before suddenly leaving the HF molecule rotationally excited. Two other examples are shown in Figs. 30 and 31. These are cases in which the H–Ca–F complex persists for about 0.5 ps before breaking up as Ca + HF. There are no apparent differences between these complexes and those in Figs. 26 and 27. Also, the role of HF rotation in promoting CaF formation observed in examination of the cross section data is not evident in the (admittedly limited) sample of trajectories examined in detail. Obviously other features, not apparent in Figs. 24–31 (e.g., overall H–Ca–F rotation) contribute to the observed cross section behavior.

VI. CONCLUSION

The studies reported herein delineate a number of predicted features of Ca + HF($v = 1$) scattering. Among these is the fact that Ca + HF constitutes an example of a neutral three atom chemical insertion reaction. Additionally, results obtained establish (1) at fixed Ca,HF initial translational energy, cross sections (both for converged CaF formation and for combined CaF formation and long-lived complex formation) increase with increasing value of the initial HF rotational quantum number J, (2) for trajectories which sample the H–Ca–F potential well, escape to form CaF + H is favored by increasing initial HF rotational energy and es-

cape to form Ca + HF is favored by increasing initial Ca,HF relative translational energies, (3) for trajectories which react in a converged fashion to form CaF, fractional product energy disposals are remarkably independent of initial collision conditions, (4) for trajectories which react in a converged fashion to form CaF, at fixed total collision energy, excitation of HF to the first excited ($v = 1$) vibrational state is much more effective in promoting CaF formation than is placing a corresponding amount of energy in initial Ca,HF translation; however, beyond $v = 1$, further HF vibrational excitation has little effect on either the cross section for converged CaF formation or the combined cross sections for converged CaF and long-lived H–Ca–F formation, and (5) for the Ca + HF reaction, a definite effect of initial HF angular momentum alignment on reactivity is observed. All these predicted behaviors are amenable to immediate experimental test and thus delineate a number of possible interesting avenues for experimental work. Additionally, the results obtained appear to support the possibility of formation of H–Ca–F complexes which behave statistically in the context of phase space theory but clearly are non-RRKM in the classical sense of internal energy randomization.

In regard to the connection between observation and the present calculations, it should again be noted that the studies reported herein were, of necessity, performed at relative translational energies in excess by ~3 kcal/mol of those used in previous experimental studies.[1] This is not felt to be a serious shortcoming. As noted in Sec. II, it is not unlikely that the *ab initio* energy barrier is too high by roughly 2 kcal/mol. If indeed this is the case, it would justify the need to use higher collision energies, and, as argued in Sec. II would in all likelihood not affect main product features and behaviors observed in the calculations. In this regard, it is encouraging to note that the low energy computed vibrational energy distributions resulting from converged reactive trajectories are in qualitative accord with low energy experimental results. The experimental results, in turn, are consistent with results obtained from phase space theory.[1] When added to converged reactive attributes, properties of nonconverged trajectories which ultimately lead to CaF formation should increase the degree of statistical behavior contributing to CaF formation and, thus, improve agreement with experiment.

It is believed that the work presented herein constitutes the best practicable first principles treatment of reactivity in Ca + HF presently available. Future experimental studies will provide an unequivocal commentary on the adequacy of this best theoretical effort.

ACKNOWLEDGMENTS

MDP expresses his gratitude to the John Simon Guggenheim Memorial Foundation for partial support of a sabbatical leave during which time the potential energy fitting and classical trajectory calculations were performed. FGM was supported by a fellowship from the Swiss National Science Foundation and RNZ thanks the US National Science Foundation, NSF CHE 84-07270, for support. MDP, FGM, and RNZ acknowledge with thank the generous grant of computer time from NASA Ames Research Center.

[1] R. Altkorn, F. E. Bartoszek, J. DeHaven, G. Hancock, D. S. Perry, and R. N. Zare, Chem. Phys. Lett. **98**, 212 (1983).
[2] C. A. Mims, S. M. Lin, and R. R. Herm, J. Chem. Phys. **57**, 3099 (1972).
[3] Z. Karny and R. N. Zare, J. Chem. Phys. **68**, 3360 (1978).
[4] Z. Karny, R. C. Estler, and R. N. Zare, J. Chem. Phys. **69**, 5199 (1969).
[5] A. Gupta, D. S. Perry, and R. N. Zare, J. Chem. Phys. **72**, 6250 (1980).
[6] D. S. Perry, A. Gupta, and R. N. Zare, *Electro-Optic Laser '80*, Proceedings (Industrial & Scientific Management, Inc., Chicago, 1981).
[7] C. K. Man and R. C. Estler, J. Chem. Phys. **75**, 2779 (1981).
[8] A. Torres-Filho and J. G. Pruett, J. Chem. Phys. **77**, 740 (1982).
[9] H. W. Cruse, P. J. Dagdigian, and R. N. Zare, Faraday Discuss. Chem. Soc. **55**, 277 (1973).
[10] J. G. Pruett and R. N. Zare, J. Chem. Phys. **64**, 1774 (1976).
[11] A. Gupta, D. S. Perry, and R. N. Zare, J. Chem. Phys. **72**, 6237 (1980).
[12] A. Torres-Filho and J. G. Pruett, J. Chem. Phys. **72**, 6736 (1980).
[13] D. L. Feldman, R. K. Lengel, and R. N. Zare, Chem. Phys. Lett. **52**, 413 (1977).
[14] A. Siegel and A. Schultz, J. Chem. Phys. **72**, 6227 (1980).
[15] C. Noda, J. S. McKillop, M. A. Johnson, J. R. Waldeck, and R. N. Zare, J. Chem. Phys. **85**, 856 (1986).
[16] H. Schor, S. Chapman, S. Green, and R. N. Zare, J. Chem. Phys. **69**, 3790 (1978).
[17] H. Schor, S. Chapman, S. Green, and R. N. Zare, J. Phys. Chem. **83**, 920 (1979).
[18] P. J. Kuntz and A. C. Roach, J. Chem. Phys. **74**, 3420 (1981).
[19] P. J. Kuntz and A. C. Roach, J. Chem. Phys. **74**, 3435 (1981).
[20] J. L. Schreiber and P. J. Kuntz, J. Chem. Phys. **76**, 1872 (1982).
[21] S. Chapman, M. Dupuis, and S. Green, Chem. Phys. **78**, 93 (1983).
[22] S. Chapman, J. Chem. Phys. **81**, 262 (1984).
[23] E. Garcia and A. Laganà, Mol. Phys. **56**, 629 (1985).
[24] M. Paniagua, J. C. Sanz, J. M. Alvarino, and A. Laganà, Chem. Phys. Lett. **126**, 330 (1986).
[25] H. Kobayashi and T. Koga, Theor. Chim. Acta **67**, 1 (1985).
[26] M. Paniagua, J. M. Garcia De La Vega, J. R. Alvarez Collodo, J. C. Sanz, J. M. Alvarino, and A. Laganà, Chem. Phys. **101**, 55 (1986).
[27] H. F. Schaefer III, J. Phys. Chem. **89**, 5336 (1985).
[28] C. W. Bauschlicher, Jr. and P. R. Taylor, J. Chem. Phys. **86**, 858 (1987).
[29] B. Liu and P. E. M. Siegbahn, J. Chem. Phys. **68**, 2457 (1978).
[30] S. P. Walch, T. H. Dunning, Jr., and R. C. Raffenetti, J. Chem. Phys. **72**, 406 (1980).
[31] T. H. Dunning, Jr., S. P. Walch, and M. M. Goodgame, J. Chem. Phys. **74**, 3482 (1981).
[32] S. R. Langhoff, C. W. Bauschlicher, Jr., and H. Partridge, in *Comparison of Ab Initio Quantum Chemistry with Experiment for Small Molecules*, edited by R. J. Bartlett (Reidel, Dordrecht, 1985), p. 357.
[33] J. A. Pople, M. J. Frisch, B. T. Luke, and J. S. Binkley, Int. J. Quantum. Chem. Symp. **17**, 307 (1983).
[34] J. Almlöf, MOLECULE, a Gaussian integral program.
[35] P. E. M. Siegbahn, C. W. Bauschlicher, Jr., B. Roos, A. Heiberg, P. R. Taylor, and J. Almlöf, SWEDEN, a vectorized SCF-MCSCF-direct CI program.
[36] B. Roos, A. Veillard, and G. Vinot, Theor. Chim. Acta **20**, 1 (1971).
[37] L. G. M. Pettersson, P. E. M. Siegbahn, and S. Ismaail, Chem. Phys. **82**, 355 (1983).
[38] N. Honjou, M. Takagi, M. Makita, and K. Ohno, J. Phys. Soc. Jpn. **50**, 2095 (1981).
[39] T. H. Dunning, Jr., J. Chem. Phys. **55**, 716 (1971).
[40] T. H. Dunning, Jr. and P. J. Hay, in *Methods of Electronic Structure Theory*, edited by H. F. Schaefer III (Plenum, New York, 1977), p. 1.
[41] P. E. M. Siegbahn, J. Almlöf, A. Heiberg, and B. O. Roos, J. Chem. Phys. **74**, 2384 (1981).
[42] S. R. Langhoff, C. W. Bauschlicher, Jr., and H. Partridge, J. Chem. Phys. **84**, 1687 (1986).
[43] F. G. Mascarello and R. L. Jaffe (unpublished results).
[44] K. P. Huber and G. Herzberg, *Molecular Spectra and Molecular Structure* (Van Nostrand Reinhold, New York, 1979).
[45] S. R. Langhoff and E. R. Davidson, Int. J. Quantum Chem. **8**, 61 (1974). See also E. R. Davidson, in *The World of Quantum Chemistry*, edited by R. Daudel and B. Pullman (Reidel, Dordrecht, 1974).
[46] B. H. Botch and T. H. Dunning, Jr., J. Chem. Phys. **76**, 6046 (1982).
[47] C. W. Bauschlicher, Jr. and P. R. Taylor, J. Chem. Phys. **85**, 2779 (1986).
[48] C. W. Bauschlicher, Jr., S. R. Langhoff, and H. Partridge, J. Chem. Phys. **84** 901 (1986).
[49] C. E. Moore, *Atomic Energy Levels*, NBS Circ. No. 467 (National Bureau of Standards, Washington, D.C., 1952).

[50]H. Hotop and W. C. Lineberger, J. Phys. Chem. Ref. Data **4**, 539 (1975).
[51]R. Grice and D. R. Herschbach, Mol. Phys. **27**, 159 (1974).
[52]$V_{att}(r_i)$ consists of all terms in $V(r_i)$ with negative sign. For the HF Morse potential it is $2D_e \exp[-\beta(r_1 - r_e)]$. For CaF and CaH it consists of the magnitude of the sum of negative terms in the lower eigenvalue of the 2×2 valence bond determinant.
[53]Even though the fitted energy is everywhere continuous, the first derivatives contain a discontinuity at $\alpha = 0°$ and 180° (the energy goes through a maximum or minimum as α goes through 0° or 180° but the first derivative is not zero). A modified potential energy expression that has continuous derivatives was prepared and tested to determine whether the results of the trajectory calculations were affected by the presence of the discontinuity. The modification consisted of replacing $1.035\,28 \sin\alpha$ in Eq. (3) by $1.053\,38 \sin^{3/2}\alpha$ and $a_2 \exp[-0.500(\pi - \alpha)]$ by $a_2 \exp[-0.785(1 + \cos\alpha)]$ and resulted in a fit to the *ab initio* energies with a root mean square deviation of 1.19 kcal/mol. Test runs of sample trajectories for several HF J values and collision energies indicated that both the original and modified potential energy fits produced very similar results with respect to all reaction attributes.
[54]D. G. Truhlar and J. T. Muckerman, in *Atom–Molecule Collision Theory—A Guide for the Experimentalist*, edited by R. B. Bernstein (Plenum, New York, 1979), Chap. 16.
[55]C. W. Gear, J. SIAM Numer. Anal. Ser. B **2**, 69 (1964).
[56]M. D. Pattengill, in *Atom–Molecule Collision Theory—A Guide for the Experimentalist*, edited by R. B. Bernstein (Plenum, New York, 1979), Chap. 10.
[57]W. C. Hamilton, *Statistics in Physical Science* (Ronald, New York, 1964), Chap. 4.
[58]M. D. Pattengill, R. N. Zare, and R. L. Jaffe, J. Phys. Chem. (submitted).
[59]See, for example, J. E. Butler, G. M. Jursich, I. A. Watson, and J. R. Wiesenfeld, J. Chem. Phys. **84**, 5365 (1986).
[60]P. A. Whitlock, J. T. Muckerman, and P. M. Kroger, in *Potential Energy Surfaces and Dynamics Calculations*, edited by D. G. Truhlar (Plenum, New York, 1981), p. 551.
[61]P. A. Whitlock, J. T. Muckerman, and E. R. Fisher, J. Chem. Phys. **76**, 4468 (1982).
[62]R. Schinke and W. A. Lester, Jr., J. Chem. Phys. **72**, 3754 (1980).